

GATE CONTROLLED CONDUCTANCE QUANTISATION IN SEMICONDUCTORS

Rahul Jo-Shua Thanasekaran

3rd Year Project Final Report

Department of Electronic &
Electrical Engineering

UCL

Supervisor: Sanjeev Kumar

8 April 2025

I have read and understood UCL's and the Department's statements and guidelines concerning plagiarism.

I declare that all material described in this report is my own work except where explicitly and individually indicated in the text. This includes ideas described in the text, figures and computer programs.

I acknowledge the assistance of the generative AI system ChatGPT-4.0 developed by OpenAI, accessible at [<https://chat.openai.com>] in summarizing my initial notes and refining my final draft.

This report contains 48 pages (excluding this page and the appendices) and 9603 words.

Signed: *Rahul Jo-Shua*
(Student)

Date: 8 April 2025

Gate Controlled Conductance Quantisation in Semiconductors

Rahul Jo-Shua Thanasekaran

This project investigates gate-controlled conductance quantisation in quantum point contacts (QPCs) using a MATLAB-based simulation framework. By modelling a smooth saddle-point potential, the study explores how discrete conductance steps emerge due to quantum confinement in one-dimensional channels. The simulation examines the influence of key physical parameters, including confinement strength (ω_y/ω_x), magnetic fields (in-plane and perpendicular), material-specific properties (effective mass and Landé g -factor), and temperature. Results show how transverse confinement enhances mode separation, while in-plane magnetic fields induce spin-resolved subbands through Zeeman splitting. Cyclotron motion under perpendicular magnetic fields introduces Landau quantisation, further stabilising conductance plateaus. The study also quantifies thermal broadening of conductance using differential analysis and FWHM (Full Width at Half Maximum) metrics. These findings align closely with theoretical expectations, offering insight into spin-resolved transport and guiding future experimental and simulation-based quantum device designs.

Table of Contents

1	Introduction & Literature Review	4
2	Theoretical & Mathematical Background	8
2.1	Creating Low-Dimensional Systems Using GaAs/AlGaAs Heterostructures .	8
2.2	Electrostatic Potential Profile and 1D Channel Formation	10
2.3	Mathematical Framework	11
3	MATLAB Software Simulation Results	14
3.1	Quantised Conductance & Mode Transmission	14
3.2	Effect of Confinement Ratio ω_y/ω_x on Conductance Quantisation	16
3.3	Transmission Probabilities and Their Influence on Conductance.....	20
3.4	Effect of an In-Plane Magnetic Field	21
3.5	Effect of a Perpendicular Magnetic Field: Cyclotron Motion and Landau Quantisation	23
3.6	Impact of Semiconductor Properties on Quantum Transport	26
3.7	Temperature Dependence of Quantised Conductance	31
4	Results Analysis & Discussion	35
4.1	Further Analysis into Confinement Ratio Relationship	36
4.2	Differential Conductance under Varying In-Plane Magnetic Fields	38
4.3	Thermal Effects on Subband Activation and Conductance Sharpness	40
5	Future Work	43
6	Conclusion	45
7	References	47
8	Appendices	50
8.1	Appendix A: MATLAB Code for Saddle-Point Potential (Figure 5).....	50
8.2	Appendix B: MATLAB Code for Split-Gate Potential Profile (Figure 6)	51
8.3	Appendix C: MATLAB Code for Fermi Energy and Thresholds (Figure 7)..	52
8.4	Appendix D: MATLAB Code for Transmission Probabilities and Total Con- ductance (Figure 8).....	53
8.5	Appendix E: MATLAB Code for Varying ω_y/ω_x (Figure 10)	54
8.6	Appendix F: MATLAB Code for Varying ω_x/ω_y (Figure 11).....	55
8.7	Appendix G: MATLAB Code for Quantised Conductance vs ω_y/ω_x (Fig- ure 12)	56
8.8	Appendix H: MATLAB Code for Transmission Probabilities (Figure 13)	57
8.9	Appendix I: MATLAB Code for In-Plane Magnetic Field Conductance (Figure 14)	59
8.10	Appendix J: MATLAB Code for Perpendicular Magnetic Field Conduc- tance (Figure 16)	61
8.11	Appendix K: MATLAB Code for Effective Mass Dependence(Figure 17)	63
8.12	Appendix L: MATLAB Code for Material-Dependent g -Factor (Figure 18) .	65

8.13	Appendix M: MATLAB Code for GaAs Electron and Hole Configurations (Figure 19)	67
8.14	Appendix N: MATLAB Code for Temperature Dependence (Figures 22, 28, 29)	69
8.15	Appendix O: MATLAB Code for Transmission Derivative (Figure 23).....	72
8.16	Appendix P: MATLAB Code for Transmission Probability vs Mode Index (Figure 24)	74
8.17	Appendix Q: MATLAB Code for Transmission Derivative vs Confinement Ratio (Figure 25)	75
8.18	Appendix R: MATLAB Code for Indexed Differential Conductance vs In- Plane Magnetic Field (Figure 26)	76

1 Introduction & Literature Review

The field of mesoscopic physics lies at the intersection of classical and quantum mechanics, where systems are large enough to contain many particles but small enough that quantum effects remain observable. These systems typically range from tens to hundreds of nanometres in size, and their transport properties are governed by the wave-like nature of electrons and coherence effects. In this regime, electrons no longer behave solely as classical particles following defined trajectories; instead, they exhibit wave properties described by their de Broglie wavelength, given by

$$\lambda = \frac{h}{p} = \frac{h}{mv} \quad (1)$$

where h is Planck's constant, p is the momentum of the particle, m is the mass of the particle and v is the velocity of the particle. When the size of the system is on the order of the de Broglie wavelength, the quantum nature of electrons becomes significant. As semiconductor devices continue to shrink, they enter the mesoscopic regime, where traditional models based on Ohm's law and diffusive transport become inadequate. Instead, quantum mechanical principles such as energy quantisation, wavefunction confinement, and tunnelling must be considered.

One of the key consequences of miniaturisation is the emergence of low-dimensional systems, where the motion of electrons is confined to one or two spatial dimensions. A notable example is the two-dimensional electron gas (2DEG), which forms at the interface of certain semiconductor heterostructures, such as GaAs/AlGaAs.

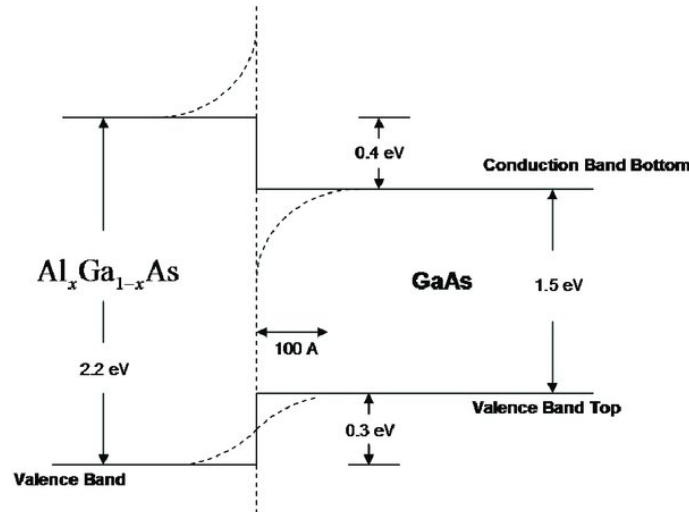


Figure 1: Band alignment in a GaAs/Al_xGa_{1-x}As heterostructure illustrating the conduction and valence band offsets that facilitate the formation of a two-dimensional electron gas (2DEG) at the interface [1]

The GaAs/AlGaAs heterostructure was chosen as the foundation for this project because it provides an ideal platform for observing and simulating quantised conductance in low-dimensional systems. Its suitability lies in its ability to support high-mobility two-dimensional electron gases, which are crucial for investigating ballistic transport and conductance quantisation in quantum point contacts (QPCs). These heterostructures

combine excellent electronic properties, mature fabrication techniques, and reliable electrostatic control.

A key mechanism enabling the formation of a 2DEG in this system is *modulation doping* [2], where the wider-bandgap AlGaAs layer is selectively doped with donors, while the adjacent GaAs layer remains undoped. Due to the conduction band offset (approximately 0.4 eV), electrons from the doped AlGaAs layer transfer to the GaAs region and accumulate near the heterointerface. This results in the formation of a thin, degenerate electron gas that is strongly confined in the vertical direction (due to the quantum well created by the band alignment) and free to move only in the two dimensions parallel to the interface.

By applying negative voltage to metallic gates on the surface of a GaAs/AlGaAs heterostructure, the two-dimensional electron gas formed at the interface can be laterally confined to create a narrow, one-dimensional conduction channel. This transition from a 2D to 1D system is the physical basis for quantised conductance: the lateral confinement leads to discrete transverse energy levels, or modes, through which electrons can propagate. Each mode contributes a fixed quantum of conductance, and as gate voltage is varied, new modes become accessible, resulting in conductance increasing in discrete steps. This fundamental mechanism underpins the operation of quantum point contacts and will be examined in more detail in the later sections.

As the semiconductor industry approaches the physical limits of miniaturisation, quantum effects that were once negligible now play a dominant role in determining device behaviour. Understanding and controlling quantum conductance is therefore critical for the design and optimisation of next-generation electronic and quantum devices. In low-dimensional systems such as quantum point contacts, the ability to manipulate electron transport at the nanoscale opens up exciting opportunities for nanoscale logic, high-sensitivity sensing, and quantum information processing.

Recent advances in the field include the use of QPCs in spin-based qubit readout [3, 4], where they act as charge sensors capable of detecting single-electron transitions in quantum dot systems with high fidelity. QPCs have also become essential tools in quantum metrology [5], where their precisely quantised conductance steps underpin resistance standards based on fundamental constants. Additionally, they are used in hybrid superconductor–semiconductor systems [6] and topological nanowires [7] to detect tunnelling events. Beyond traditional GaAs platforms, new material systems like graphene [8] and transition metal dichalcogenides (TMDs) [9] are being explored for their atomically thin structures, gate tunability, and compatibility with low-dimensional transport. Advances in fabrication techniques and cryogenic electronics have further enabled the observation of quantised conductance under complex conditions, including spin-orbit coupling and superconducting proximity effects.

A key advantage of these systems is the tunability provided by gate voltages, which enables dynamic control over the confinement potential and the number of conducting modes within the channel. This level of control is not only essential for studying funda-

mental quantum transport phenomena, such as conductance quantisation, but also for the realisation of scalable and reconfigurable nanostructures. Simulation-based approaches provide a valuable framework for visualising and predicting electronic behaviour prior to fabrication. By modelling the electrostatic potential and calculating transmission and conductance characteristics, simulations offer insight into device performance, guide experimental design, and reduce trial-and-error in the fabrication process. As we transition further into the quantum era of electronics, such tools and models become indispensable for both academic research and technological development.

The phenomenon of quantised conductance was first experimentally observed in 1988 by two independent research groups: van Wees et al. [10] and Wharam et al. [11]. Their groundbreaking work demonstrated that, in a QPC, conductance increases in discrete steps of $2e^2/h$ as a function of gate voltage, confirming the quantisation of conductance in one-dimensional channels. Since then, QPCs have become a central platform for exploring mesoscopic transport and quantum confinement. To model the underlying electrostatic environment, Büttiker and collaborators introduced the saddle-point potential [12], which provides an analytical approximation of the confining potential landscape within a QPC. This approach remains one of the foundational models in the study of quantum transport, forming the theoretical basis of this report.

The saddle-point model describes a potential that is parabolic in the transverse direction and inverted parabolic in the transport direction, allowing a semi-analytical treatment of electron transmission and conductance. Technological advancements in split-gate fabrication and electron-beam lithography have further enabled the practical realisation of QPCs in high-mobility 2DEGs, commonly formed at the interface of GaAs/AlGaAs heterostructures. These systems exhibit low disorder and strong electrostatic control, making them ideal for observing quantised conductance and other quantum transport phenomena.

Although much of the literature focuses on experimental investigations, simulation-based studies are equally important for understanding the idealised behaviour of QPCs. Experimental systems are inherently limited by temperature effects, material imperfections, and fabrication inconsistencies. In contrast, simulations offer the ability to model perfect, noise-free environments and isolate key physical parameters. Furthermore, this work adopts a more realistic, continuous saddle-shaped potential to better replicate the gradual transition between conductance plateaus. This approach not only aligns with the foundational Büttiker model but also allows detailed exploration of how gate voltages control transmission and conductance at the nanoscale.

In this project, a MATLAB-based simulation is developed to model electron transport through a gate-defined QPC using a smooth saddle-point potential. The aim is to explore how conductance quantisation is influenced by various parameters, including the confinement strength (i.e., the ratio ω_y/ω_x), material-specific properties such as effective mass and g-factor, the application of a magnetic field (i.e., in-plane and perpendicular B-field), and temperature-dependent effects. This simulation-based approach enables visualisation and analysis of idealised quantum transport behaviour, building directly on the foundational models described above while offering insights into how tunable external conditions

shape conductance in low-dimensional semiconductor systems.

To achieve these goals, the project sets out the following objectives, each designed to extend or build upon existing theoretical and experimental frameworks:

Project Objectives:

- To simulate electron transport through a QPC using a realistic, continuous saddle-point potential, extending Büttiker's [12] foundational model.
- To model how varying gate voltages reshape the electrostatic landscape and influence the opening of discrete conduction modes, as originally observed by van Wees [10] and Wharam [11].
- To explore how the ratio of transverse to longitudinal confinement (ω_y/ω_x) affects conductance, capturing how gate geometry impacts quantisation.
- To study the effect of an external magnetic field on quantised conductance and mode degeneracy, relevant to studies of Landau levels and spin-resolved transport.
- To analyse the impact of material-specific properties such as the effective mass and g-factor, particularly in GaAs/AlGaAs systems.
- To evaluate the temperature dependence of conductance quantisation and thermal smearing of plateaus, reflecting real-world experimental conditions.
- To visualise transmission functions and conductance steps for different physical scenarios, enabling comparison with analytical predictions and experimental trends.

2 Theoretical & Mathematical Background

2.1 Creating Low-Dimensional Systems Using GaAs/AlGaAs Heterostructures

Electrons inherently exist and move freely in three dimensions. However, the aim of this project is to study their behaviour when they are progressively confined to one dimension. Achieving this requires a carefully engineered structure that limits electron motion in two directions while allowing free propagation along the remaining axis.

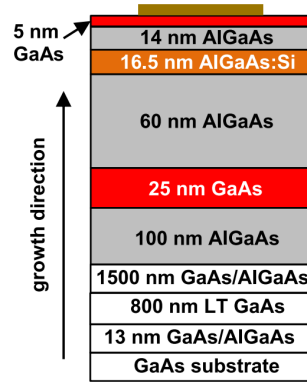


Figure 2: Schematic of the GaAs/AlGaAs heterostructure forming a 2DEG [13]

The first step involves the fabrication of a semiconductor heterostructure, typically composed of GaAs/AlGaAs, as shown in Figure 2. Due to the conduction band offset between the two materials, electrons from the doped AlGaAs layer migrate into the adjacent undoped GaAs layer, where they accumulate at the interface. This results in the formation of a two-dimensional electron gas — a nanometre-thick conducting layer in which electrons are strongly confined in the growth direction (typically the z -axis) due to the band bending and quantum well at the heterointerface. The electron motion becomes quantised in this confined direction, and only the lowest subband is typically occupied at low temperatures, leaving electrons free to move only within the x - y plane.

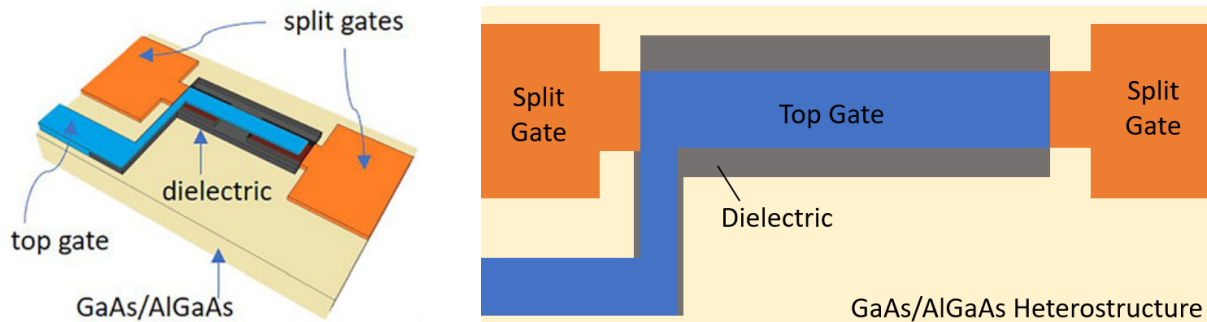


Figure 3: Schematic diagrams of a gate-defined quantum point contact structure formed on a GaAs/AlGaAs heterostructure. Left: 3D perspective showing the arrangement of split gates and a top gate separated by a dielectric layer. Right: Cross-sectional view highlighting the layered architecture, including the split gates used to define the QPC channel and the top gate used to modulate carrier density in the two-dimensional electron gas beneath [14–17]

Next, a patterned circuit is fabricated on top of this heterostructure using lithography, as shown in Figure 3. Metallic contacts are defined to act as the source and drain,

enabling the injection and collection of electrons within the 2DEG. This setup allows for well-controlled electron flow within the plane of the interface.

The final step introduces lateral confinement. By applying negative voltages to split metallic gates placed on the surface, an electric field is induced that depletes the 2DEG beneath the gates. As the voltage increases, the depleted regions grow and begin to constrict the conducting channel from the sides. This lateral squeezing of the electron gas confines electron motion in the transverse direction (typically the y -axis), forming a narrow conduction path along the transport direction (x -axis). When the channel width becomes comparable to the electron's Fermi wavelength, the electron motion becomes quantised in the transverse direction as well. The system now behaves as a quasi-one-dimensional [18] conductor, where the energy levels in the confined direction form discrete subbands or transverse modes.

Each of these modes represents a quantised standing wave in the lateral direction. Electrons can only transmit through the channel if their energy exceeds the threshold of a given mode. As a result, conductance through the channel occurs in discrete steps, with each open mode contributing one quantum of conductance, ideally $2e^2/h$ when spin degeneracy is preserved. This transition from a continuous 2D energy spectrum to discrete 1D modes is the fundamental mechanism underlying quantised conductance, a phenomenon explored and simulated throughout this project.

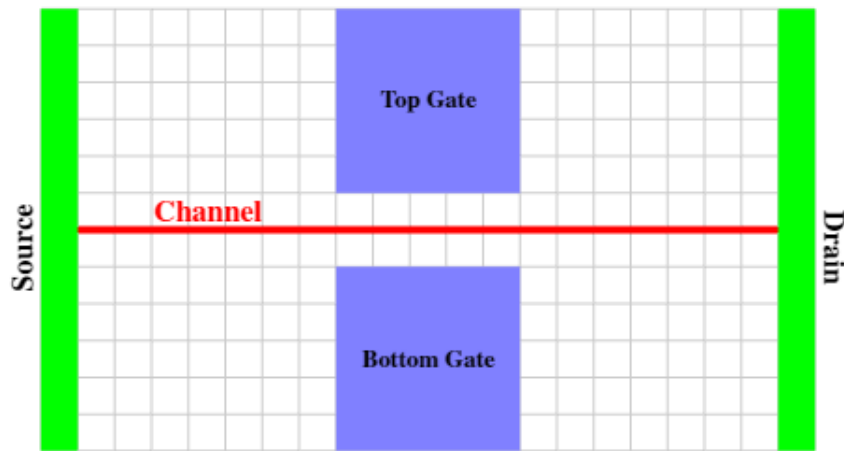


Figure 4: Simplified schematic of split-gate technology. Green indicates source and drain, red shows the 2DEG channel, and blue gates control electron flow by creating a constriction [19]

Figure 4 shows a simplified model of a one-dimensional electron channel defined within a 2DEG. The source and drain contacts provide the entry and exit points for electrons traveling through the channel, which is confined laterally by gate voltages. It is important to note that all experiments are conducted at cryogenic temperatures (i.e., approximately -273°C or 0 K) to suppress thermal noise and enhance quantum effects.

2.2 Electrostatic Potential Profile and 1D Channel Formation

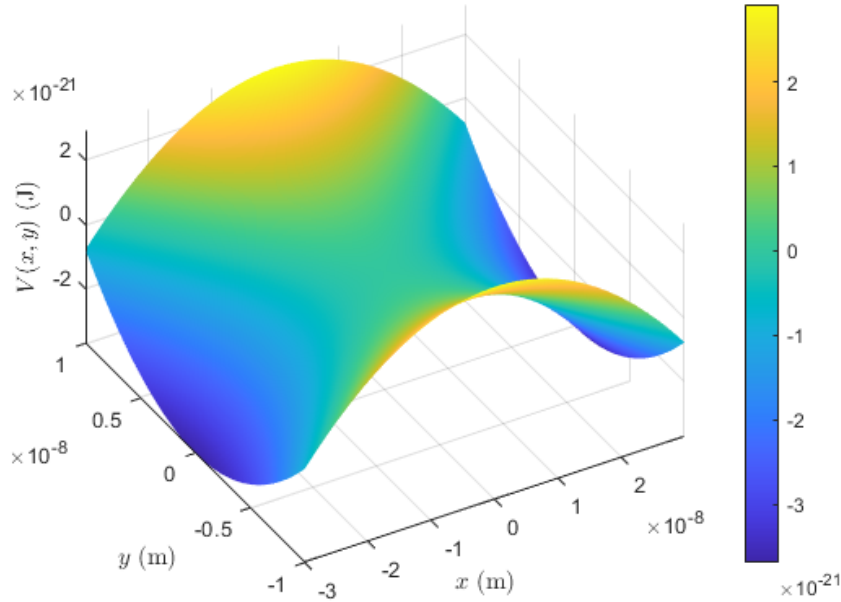


Figure 5: Simulated saddle-shaped electrostatic potential used to model the effect of gate voltages in a quantum point contact (Appendix 8.1)

As this project is simulation-based, the effect of gate voltages is modeled by introducing a saddle-shaped electrostatic potential seen in Figure 5 adopted from [12], which mimics the confinement and transport characteristics of electrons in a QPC. The potential is defined as:

$$V(x, y) = V_0 - \frac{1}{2}m\omega_x^2x^2 + \frac{1}{2}m\omega_y^2y^2 \quad (2)$$

1. V_0 : The baseline potential, set by external gate voltages, defining the overall height of the potential.
2. $-\frac{1}{2}m\omega_x^2x^2$: The parabolic term along the x -axis, representing a potential barrier that constrains electron motion. Here, m is the effective electron mass, and ω_x is the angular frequency determining the barrier curvature in the x -direction.
3. $+\frac{1}{2}m\omega_y^2y^2$: The parabolic term along the y -axis, representing a confining potential well. Similarly, m is the effective mass of the electron, and ω_y is the angular frequency that governs the curvature of the well in the y -direction.

Varying ω_x and ω_y controls the shape of the saddle potential. Increasing ω_x steepens the barrier along the transport direction, effectively shortening the channel, while decreasing it makes the channel longer and smoother. Similarly, increasing ω_y tightens confinement in the transverse direction, narrowing the channel width and reducing the number of conducting modes. Together, these parameters allow tuning of the channel's shape and quantum transport properties.

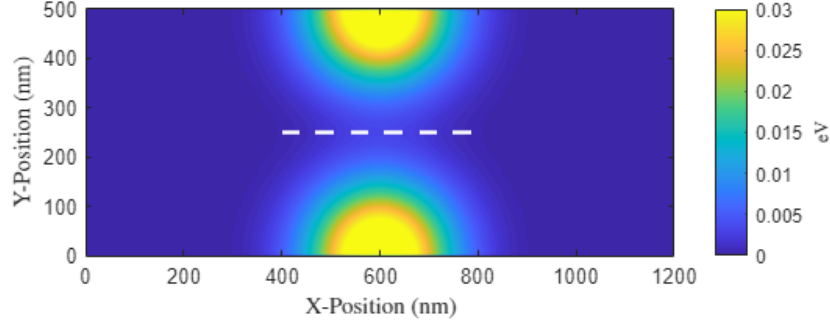


Figure 6: Simulated electrostatic potential profile in the x-y plane, illustrating a saddle-shaped confinement. The white dashed line highlights the region along the channel which is evaluated for further analysis. The colour scale represents the potential energy in electron volts (eV) (Appendix 8.2)

This saddle-point potential closely replicates the electrostatic landscape formed in real QPC devices when gate voltages are applied, as shown in Figure 6, allowing investigation of quantum transport phenomena within a one-dimensional channel. It's easier to see here that as the gate voltage is swept, the potential gradually pinches the channel, reducing its width and increasing lateral confinement. The transition to a one-dimensional channel is observed in the vicinity of the dotted white line region.

2.3 Mathematical Framework

Before being able to conduct simulations, a base mathematical framework was developed to accurately describe the physical behaviour of the system.

Hamiltonian of the System

To study the quantum behaviour of electrons in the saddle potential, we begin with the time-independent Schrödinger equation:

$$H\Psi(x, y) = E\Psi(x, y) \quad (3)$$

where H is the Hamiltonian operator, E is the total energy, and $\Psi(x, y)$ is the wavefunction of the system.

The Hamiltonian includes both kinetic and potential energy contributions [20]:

$$H = \frac{p_x^2}{2m} + \frac{p_y^2}{2m} + V(x, y) \quad (4)$$

where p_x and p_y are the momentum operators in the x - and y -directions respectively, m is the effective mass of the electron, and $V(x, y)$ is the electrostatic potential energy landscape experienced by the electron due to external gate voltages.

Substituting the momentum operators and the defined saddle potential into the Hamiltonian, we get:

$$H = -\frac{\hbar^2}{2m} \left(\frac{\partial^2}{\partial x^2} + \frac{\partial^2}{\partial y^2} \right) + V_0 - \frac{1}{2}m\omega_x^2 x^2 + \frac{1}{2}m\omega_y^2 y^2 \quad (5)$$

Here, the kinetic energy is expressed in terms of the second derivatives of the wavefunction, and the potential energy consists of a constant offset V_0 , an inverted parabolic term in the x -direction, and a regular parabolic term in the y -direction, resulting in a saddle-shaped electrostatic landscape as mentioned earlier.

To solve the Schrödinger equation, we assume the potential is separable in x and y , which allows the total wavefunction to be written as a product of two independent functions:

$$\Psi(x, y) = \psi_x(x)\psi_y(y) \quad (6)$$

This separability enables us to treat each direction independently. We begin by solving the equation in the y -direction, where the potential has a quadratic form corresponding to a one-dimensional harmonic oscillator. The resulting equation is:

$$H_y\psi_y(y) = E_y\psi_y(y) \quad (7)$$

where the y -component of the Hamiltonian is given by:

$$H_y = -\frac{\hbar^2}{2m} \frac{d^2}{dy^2} + \frac{1}{2}m\omega_y^2 y^2 \quad (8)$$

This is the well-known Hamiltonian of the quantum harmonic oscillator. Its solutions are well established, with quantised energy levels given by:

$$E_y = \hbar\omega_y \left(n + \frac{1}{2} \right), \quad n = 0, 1, 2, \dots \quad (9)$$

These energy levels arise due to the confining potential in the transverse (y) direction. Each integer n represents a discrete transverse mode that an electron can occupy.

Once the transverse energy E_y is known, we can determine the longitudinal energy E_x , which is the remaining energy available to the electron for motion in the transport (x) direction. Since total energy is conserved, we write:

$$E = E_x + E_y \quad \Rightarrow \quad E_x = E - \hbar\omega_y \left(n + \frac{1}{2} \right) \quad (10)$$

This expression shows that for each transverse mode n , the energy available for transport decreases by the quantised transverse energy. As a result, only modes for which $E > E_y$ contribute to conduction, while higher modes become inaccessible when the total energy is too low.

Scaled Energy Parameter

To analyse transmission and improve quality of results, we define a dimensionless energy parameter:

$$\epsilon_n = \frac{2(E - \hbar\omega_y(n + 0.5) - V_0)}{\hbar\omega_x} \quad (11)$$

This compares the effective kinetic energy in the x -direction to the barrier curvature governed by ω_x . It also serves as a convenient dimensionless parameter for plotting, as it

transforms energy into a scaled form where meaningful features appear at relatively small and interpretable values, often close to integers, rather than large or arbitrary absolute energy values.

Transmission Probability and Conductance

The transmission probability for each transverse mode n is given by:

$$T_n = \frac{1}{1 + \exp(-\pi\epsilon_n)} \quad (12)$$

This expression describes how likely it is for an electron in mode n to transmit through the saddle-shaped potential barrier. The value of T_n depends on the scaled energy parameter ϵ_n , which measures how far the electron's energy lies above or below the barrier.

As $\epsilon_n \rightarrow \infty$, the electron energy greatly exceeds the potential barrier, resulting in:

$$T_n \rightarrow 1$$

This corresponds to *full transmission*, where the mode is fully open and contributes maximally to conductance.

In contrast, as $\epsilon_n \rightarrow -\infty$, the electron energy is well below the barrier height, and:

$$T_n \rightarrow 0$$

This represents *zero transmission*, where the mode is completely closed and does not contribute to current flow.

Therefore, T_n provides a smooth transition between closed and open quantum channels as energy increases, forming the basis for quantised conductance behaviour.

The total quantum conductance is given by summing over all available modes:

$$G = \sum_n T_n \frac{e^2}{h} \quad (13)$$

This reflects quantised conductance in units of e^2/h , with smooth transitions between steps due to the saddle potential geometry.

With the theoretical framework and governing equations now established, we can implement the simulation in MATLAB to numerically model electron transport through the quantum point contact.

3 MATLAB Software Simulation Results

3.1 Quantised Conductance & Mode Transmission

In one-dimensional quantum systems, such as those formed in a quantum point contact, electron transport exhibits behaviour fundamentally different from that in classical conductors. This is due to quantum confinement: when electrons are laterally confined to a narrow constriction, their motion perpendicular to the transport direction becomes quantised. In this case, quantum confinement is achieved through the use of a semiconductor heterostructure (GaAs/AlGaAs) combined with electrostatic gating, which together define a narrow, one-dimensional channel within a two-dimensional electron gas. This confinement leads to the formation of discrete energy levels known as transverse modes or subbands.

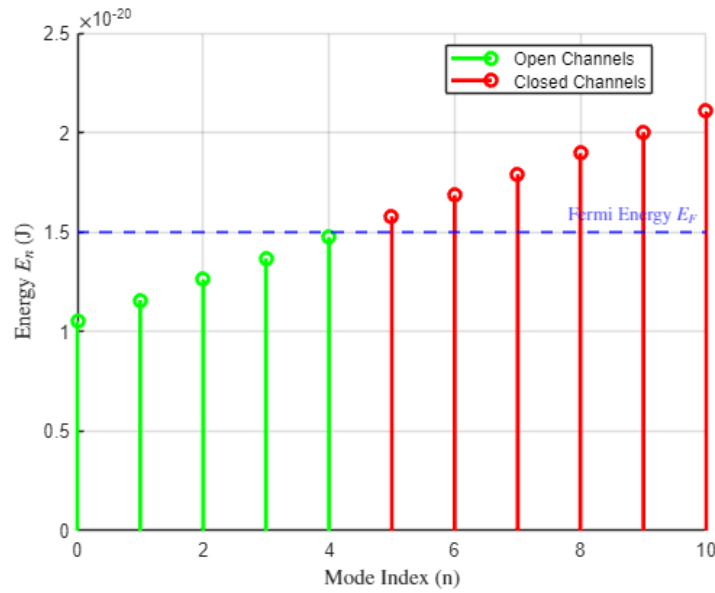


Figure 7: Transmission of transverse modes relative to the Fermi energy E_F . Green bars represent open channels ($E_n < E_F$) that contribute to conductance, while red bars indicate closed channels ($E_n > E_F$) that are energetically inaccessible. The horizontal dashed line marks the Fermi level, determining which modes are active in transport (Appendix 8.3)

Each of these modes represents a standing wave solution in the confined direction. For a given mode to contribute to conductance, its threshold energy must lie below the Fermi energy, as illustrated in Figure 7. In this way, the QPC acts like a tunable filter, allowing electrons to pass through only if they occupy accessible modes. The longitudinal motion of the electron (i.e., along the transport direction) remains continuous, but only certain transverse wavefunctions are allowed, creating a discrete set of conducting modes in the channel.

The quantisation of conductance arises from this mode structure. Each mode that is fully open (i.e., its threshold energy lies below the Fermi energy) contributes a fixed amount of conductance:

$$G_n = T_n \frac{e^2}{h} \quad (14)$$

where T_n is the transmission probability of the n -th mode. In the ideal case at zero temperature, $T_n = 1$ for open modes and $T_n = 0$ for closed ones. Therefore, each open mode contributes one full quantum unit of conductance, e^2/h . Thus, the total conductance is then given by the sum over all modes:

$$G = \sum_n T_n \frac{e^2}{h} \quad (15)$$

If spin degeneracy is preserved [21], each conducting mode contributes $2e^2/h$ to the total conductance. Spin degeneracy refers to the quantum mechanical property that allows each spatial electron state to be occupied by two electrons with opposite spin orientations: one spin-up and one spin-down. In the absence of external magnetic fields or spin-dependent interactions, these spin states are energetically degenerate—meaning they have the same energy and are equally likely to contribute to transport. As a result, for every allowed transverse mode, two independent spin channels can transmit electrons through the quantum point contact. This effectively doubles the conductance contribution of each mode from e^2/h to $2e^2/h$, as seen in Equation 16, leading to the characteristic quantised conductance steps observed in ideal one-dimensional systems. For consistency, conductance values throughout this report are expressed in units of e^2/h when spin-degenerate.

The total conductance through the QPC, assuming spin degeneracy is preserved, is given by the sum over all modes, each weighted by its transmission probability:

$$G = \sum_n T_n \frac{2e^2}{h} \quad (16)$$

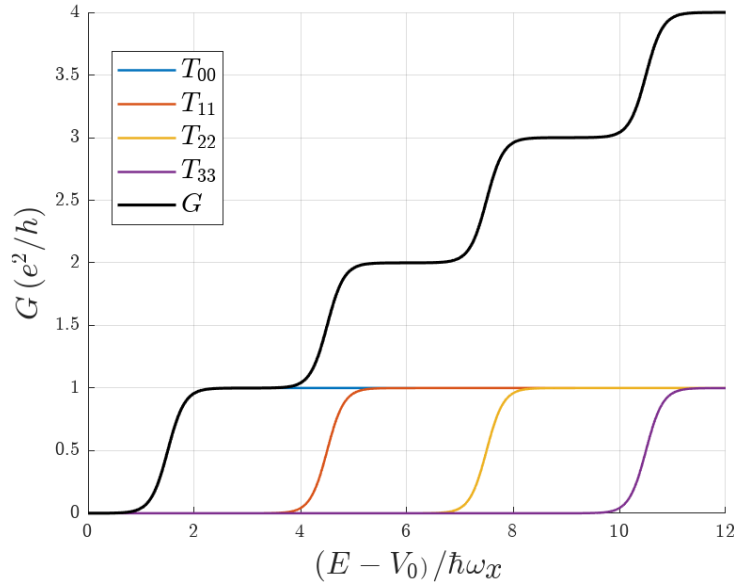


Figure 8: Quantised conductance and individual mode transmission as a function of scaled energy. The black curve represents the total conductance G , calculated as the sum of the transmission probabilities T_n of each mode. The coloured curves show the transmission functions for the first four transverse modes ($T_{00}, T_{11}, T_{22}, T_{33}$). Each mode transitions smoothly from 0 to 1 as its threshold energy is exceeded, resulting in the characteristic staircase profile in G (Appendix 8.4)

As the Fermi energy increases (e.g., through gate voltage tuning), more transverse modes become energetically accessible. Each mode gradually transitions from fully closed ($T_n = 0$) to fully open ($T_n = 1$), leading to discrete steps in conductance. This behaviour can be demonstrated in simulation by sweeping the energy across a range and observing how each mode contributes to the total conductance as it becomes active as seen above in Figure 8. This staircase-like behaviour reflects the quantised nature of electron transport in 1D systems. The sharpness of these steps depends on various factors, including confinement ratios, the presence of a magnetic field, material properties, and temperature. These influences determine how gradually or abruptly each mode transitions from closed to open. These factors will be deeper looked into in the later sections.

3.2 Effect of Confinement Ratio ω_y/ω_x on Conductance Quantisation

In the saddle-point model used earlier in Equation 2 to describe a quantum point contact, the electrostatic potential is given by:

$$V(x, y) = V_0 - \frac{1}{2}m\omega_x^2x^2 + \frac{1}{2}m\omega_y^2y^2$$

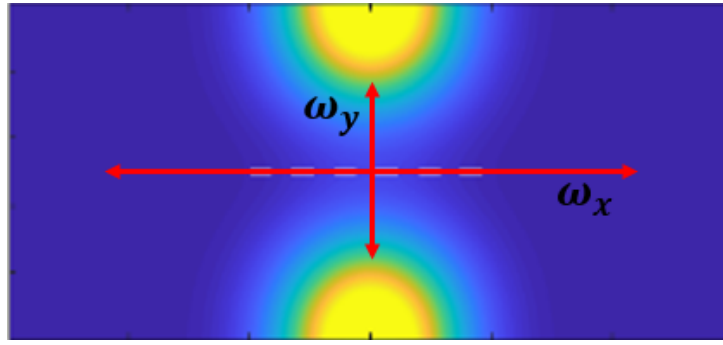


Figure 9: Schematic representation of a saddle-point potential, showing the characteristic confinement strengths ω_y and ω_x along the transverse and longitudinal directions, respectively

Here, ω_x controls the curvature of the potential barrier along the transport direction (longitudinal), while ω_y determines the strength of confinement in the transverse direction. The ratio ω_y/ω_x is therefore a key parameter that shapes the saddle-point potential and plays a crucial role in determining the system's conductance behaviour.

This confinement ratio dictates the relative sharpness of mode thresholds and directly impacts the *clarity*, *separation*, and *flatness* of conductance plateaus. A low confinement ratio ($\omega_y/\omega_x \approx 1$) corresponds to a saddle that is relatively shallow in the transverse direction. In such configurations, the transverse modes are not tightly confined, leading to small energy spacing between adjacent subbands. As a result, their transmission functions overlap significantly, causing the conductance to increase smoothly without forming distinct steps — a hallmark of poorly defined quantisation.

In contrast, a higher confinement ratio steepens the potential in the transverse direction. This pushes the subband energies further apart, reducing overlap between modes and leading to sharper, more distinct transitions in conductance. The conductance plateaus

become flatter and broader, which means that conductance remains nearly constant over a larger range of energies. This reduced sensitivity to small energy variations — or gate voltage fluctuations — is what makes the system more *stable* in a practical and measurable sense.

In this context, a **stable system** is defined as one in which the conductance steps are:

- Well-defined and evenly spaced,
- Separated by wide, flat plateaus, and
- Less sensitive to small changes in Fermi energy.

Such stability is essential for both experimental reproducibility and device design. The condition for achieving this regime is typically:

$$\omega_y \gg \omega_x$$

To test this hypothesis, simulations were performed by sweeping the Fermi energy at fixed ω_x for different values of ω_y . Figures 10 & 11 shows the resulting conductance profiles for $\omega_y/\omega_x = 1, 2, 3$, and 4. As the ratio increases, the steps in conductance become increasingly sharp and the plateaus more pronounced. At $\omega_y/\omega_x = 3$ and 4, the conductance shows clearly defined quantisation with longer plateau regions, demonstrating the stabilising effect of stronger transverse confinement.

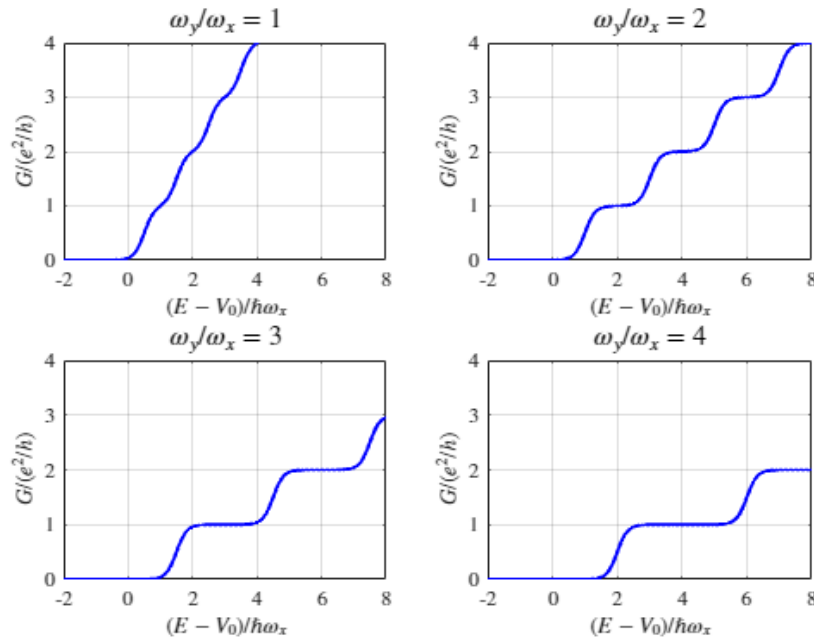


Figure 10: Simulated quantised conductance as a function of scaled energy $(E - V_0)/\hbar\omega_x$ for different transverse confinement strengths ω_y , with ω_x held constant. Each subplot corresponds to a different confinement ratio $\omega_y/\omega_x = 1, 2, 3$, and 4 (Appendix 8.5)

Figure 10 shows that as ω_y increases while ω_x is held constant, the transverse confinement becomes stronger, which increases the energy separation between transverse modes.

This enhanced mode separation means that each mode becomes energetically distinct, reducing overlap in their transmission probabilities. As a result, the conductance plateaus become wider and flatter, and the transitions between them sharper (improved quantisation). The smoother, more well-defined steps indicate that the system exhibits greater stability, as the conductance remains less sensitive to small changes in Fermi energy or gate voltage. Physically, stronger transverse confinement ensures that electrons occupy well-localised modes within the constriction, allowing each mode to turn on individually and contributing to the clean, stepwise nature of the quantised conductance.

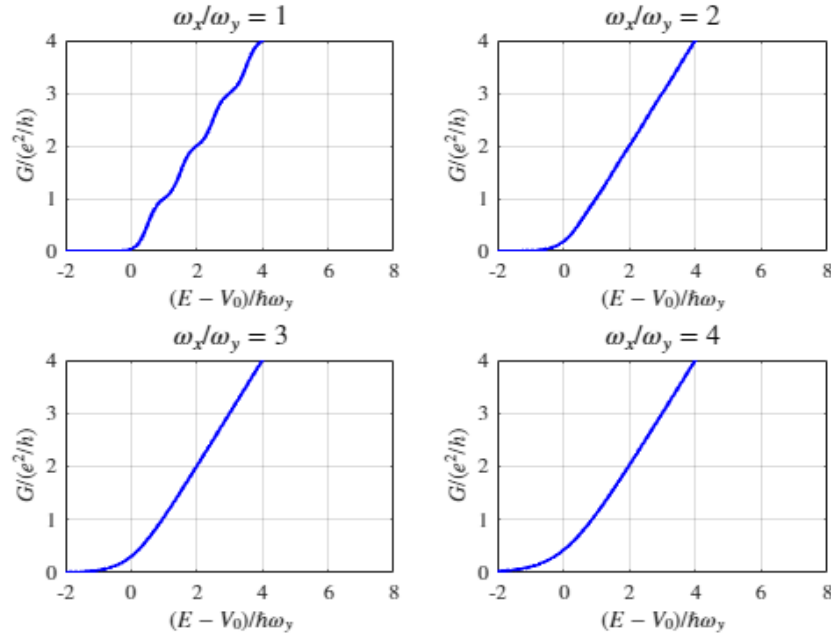


Figure 11: Simulated quantised conductance as a function of scaled energy $(E - V_0)/\hbar\omega_y$ for different longitudinal potential curvatures ω_x , with ω_y held constant. Each subplot corresponds to a different inverse confinement ratio $\omega_x/\omega_y = 1, 2, 3$, and 4 (Appendix 8.6)

As ω_x increases, the curvature of the potential along the transport direction becomes steeper, resulting in a narrower and sharper barrier through which electrons must propagate. At $\omega_x/\omega_y = 1$, the conductance exhibits clear, step-like behaviour, characteristic of ideal quantised conductance. However, as ω_x increases, the conductance steps gradually smear out and the staircase structure is lost. This is because a steeper potential reduces the spatial region over which electrons are injected into the channel, which increases the likelihood of coupling between modes—particularly when the energy separation between them is small. This effect, known as *mode mixing*, causes the transmission functions of adjacent modes to overlap significantly.

The cumulative result is a conductance profile that increasingly resembles a linear ramp rather than a set of quantised steps. Multiple modes begin to contribute simultaneously and continuously, which leads to a smooth, almost uniform increase in conductance with energy. This behaviour indicates a departure from ideal quantisation and reflects diminished mode separation and system stability. The results emphasise the importance of a gently varying potential in the transport direction (i.e., smaller ω_x) to ensure clean,

independent mode activation and preserve the quantised conductance plateaus.

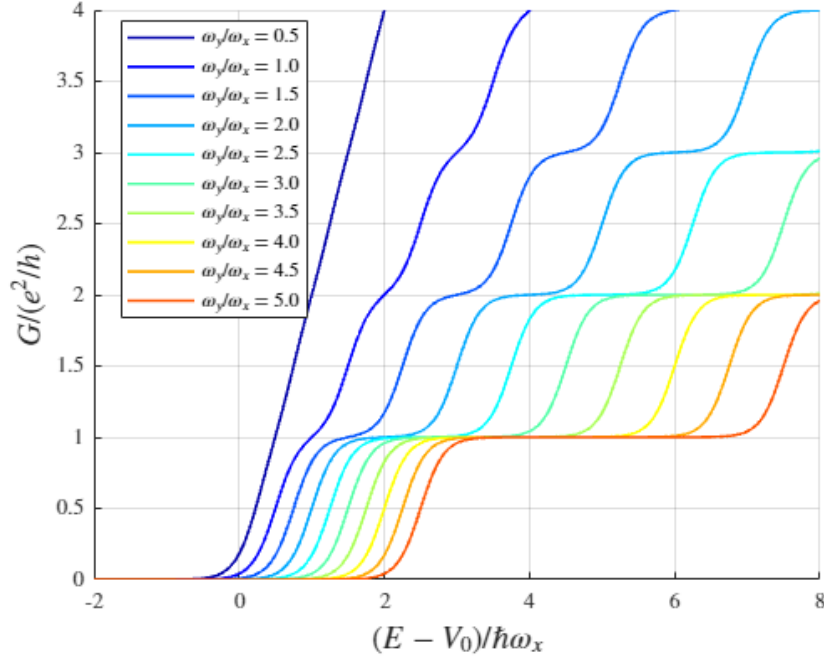


Figure 12: Simulated quantised conductance as a function of scaled energy $(E - V_0)/\hbar\omega_x$ for various confinement ratios ω_y/ω_x (Appendix 8.7)

As seen in Figure 12, higher ratios (e.g., the red curve corresponding to $\omega_y/\omega_x = 5.0$) exhibit more well-defined quantisation with extended plateau regions, indicating enhanced mode separation and improved system stability compared to the rest. Together, these results demonstrate that both increasing ω_y and decreasing ω_x —that is, increasing the overall confinement ratio—lead to sharper conductance steps and wider plateaus.

3.3 Transmission Probabilities and Their Influence on Conductance

In an ideal one-dimensional system, each transverse mode contributes a full quantum of conductance ($2e^2/h$) when the transmission probability $T_n = 1$. However, in practical scenarios, transmission is often less than perfect due to several underlying physical effects. These include:

- **Scattering from disorder or impurities:** Real semiconductor structures contain imperfections, such as lattice defects, interface roughness, or residual impurities, all of which can scatter electrons and reduce their likelihood of transmitting cleanly through the constriction.
- **Abrupt or non-adiabatic potential changes:** If the potential landscape changes too rapidly along the transport direction, electrons may reflect or couple into other modes, resulting in transmission probabilities below unity.
- **Partial tunnelling near mode thresholds:** When an electron's energy is near the threshold for a given transverse mode, it may only partially transmit through the channel. This leads to a gradual turn-on of each mode rather than an abrupt step.

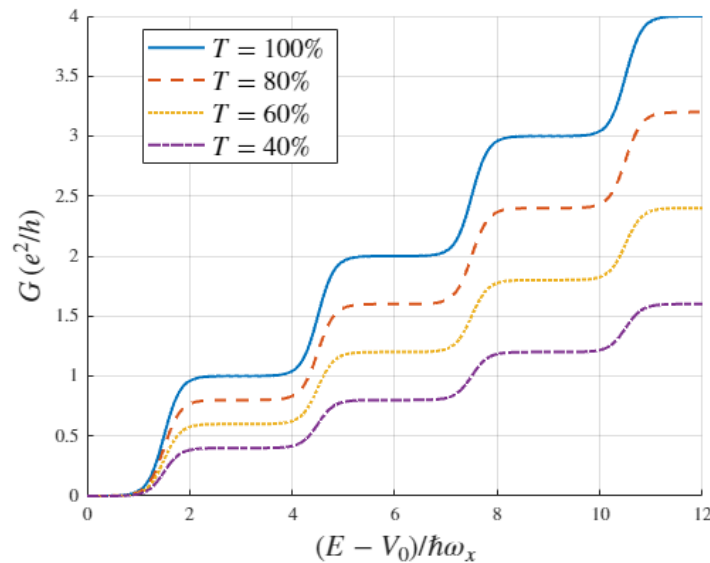


Figure 13: Simulated conductance for various maximum transmission probabilities: 100%, 80%, 60%, and 40%. As transmission decreases, each conductance step becomes less pronounced and the quantised plateaus are suppressed, reflecting increased scattering or tunnelling effects (Appendix 8.8)

As shown in Figure 13, decreasing the maximum transmission probability causes each conductance step to become less pronounced. The overall shape of the conductance staircase is preserved, but the plateaus are suppressed and flattened. Instead of clean steps, the conductance now rises more gradually with energy, reflecting the fact that electrons are not fully transmitted through each mode.

This demonstrates that quantised conductance is robust but sensitive to the quality of transmission. Even small deviations from perfect transmission reduce the clarity of the quantised steps, especially at higher modes where cumulative effects of scattering and tunnelling are more significant. Therefore, engineering high-transparency quantum point contacts with smooth, controlled confinement profiles and minimal disorder is essential to preserve well-defined quantisation.

3.4 Effect of an In-Plane Magnetic Field

In quantum point contacts, the conductance is quantised in discrete steps as electrons pass through one-dimensional modes. In the absence of a magnetic field, each mode is spin-degenerate, meaning both spin-up and spin-down electrons occupy the same energy level. As a result, each fully transmitted mode contributes $2e^2/h$ to the total conductance.

When an external *in-plane magnetic field* (B_{\parallel}) is applied [22], the degeneracy is lifted due to the *Zeeman effect* [23]. This effect arises from the interaction between an electron's intrinsic magnetic moment—associated with its spin—and the external magnetic field. The magnetic moment of an electron is given by:

$$\mu = -g\mu_B \frac{S}{\hbar} \quad (17)$$

where g is the g-factor, μ_B is the Bohr magneton, and S is the spin angular momentum.

When a magnetic field is applied, this interaction results in a splitting of the energy levels for spin-up and spin-down electrons. The magnitude of this energy splitting is:

$$E_Z = \pm \frac{1}{2} g\mu_B B_{\parallel} \quad (18)$$

This spin splitting separates each transverse subband into two distinct levels, one for each spin orientation. Consequently, each mode now contributes up to e^2/h per spin channel, resulting in smaller, more frequent steps in the conductance staircase.

In this simulation, the magnetic field is applied in the plane of the 2DEG, parallel to the transport direction. The resulting energy levels for each spin state are shifted by the Zeeman term, modifying the transverse confinement energies as follows:

$$E_n^{(s)} = \hbar\omega_y \left(n + \frac{1}{2} \right) + V_0 + \frac{s}{2} g\mu_B B_{\parallel} \quad (19)$$

where $s = +1$ for spin-up and $s = -1$ for spin-down. The transmission probability for each mode is calculated as before in terms of scaled energy:

$$T_n^{(s)} = \frac{1}{1 + \exp\left(-\pi\epsilon_n^{(s)}\right)}, \quad \epsilon_n^{(s)} = \frac{E - E_n^{(s)}}{\hbar\omega_x} \quad (20)$$

The total conductance is then obtained by summing over all spin and mode contributions:

$$G = \sum_n (T_n^{\uparrow} + T_n^{\downarrow}) \frac{e^2}{h} \quad (21)$$

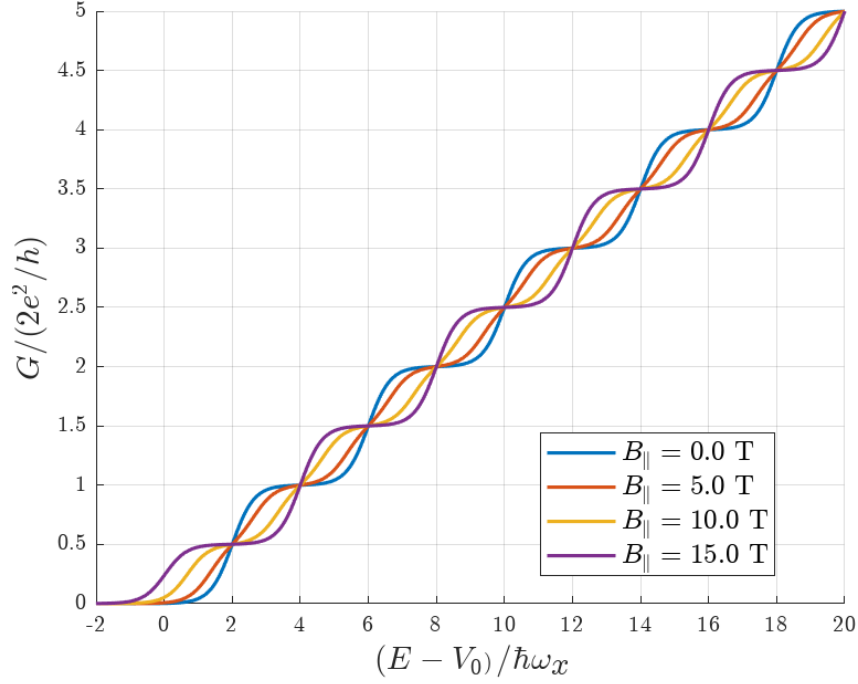


Figure 14: Simulated conductance for different in-plane magnetic field strengths ($B_{\parallel} = 0, 5, 10,$ and 15 T) at a fixed confinement ratio of $\omega_y/\omega_x = 4$. As B_{\parallel} increases, the Zeeman effect lifts spin degeneracy, resulting in the splitting of each conductance step. This produces smaller, evenly spaced steps of height e^2/h , rather than the $2e^2/h$ steps seen at zero field (Appendix 8.9)

The simulation results in Figure 14 clearly show the evolution of conductance under varying in-plane magnetic field strengths. At $B_{\parallel} = 0$ T, the expected staircase structure of quantised conductance is observed, with each step corresponding to a contribution of $2e^2/h$. As the magnetic field increases to 5 T, 10 T, and 15 T, each plateau splits due to the lifted spin degeneracy. This results in finer conductance steps of e^2/h , producing a more densely spaced staircase that reflects the spin-resolved subband structure.

In the simulation, this behaviour is particularly evident when plotting the conductance in units of $2e^2/h$. As the spin degeneracy is lifted, the height of each conductance step decreases from 1 unit to 0.5 units, clearly illustrating the transition from spin-degenerate to spin-resolved transport [24].

3.5 Effect of a Perpendicular Magnetic Field: Cyclotron Motion and Landau Quantisation

When a magnetic field is applied *perpendicular* to the plane of a two-dimensional electron gas, the motion of electrons is fundamentally altered due to the action of the Lorentz force. Unlike an in-plane magnetic field, which affects spin degeneracy, a perpendicular field leads to quantisation of the electron's orbital motion into discrete energy levels known as *Landau levels*. This has a profound impact on the conductance behaviour of a quantum point contact.

Lorentz Force and Cyclotron Motion

The motion of a charged particle in a magnetic field is governed by the Lorentz force:

$$\mathbf{F} = -e(\mathbf{v} \times \mathbf{B}) \quad (22)$$

where \mathbf{F} is the force, e is the elementary charge, \mathbf{v} is the velocity, and \mathbf{B} is the magnetic field vector. For a magnetic field applied perpendicular to the 2DEG ($\mathbf{B} = B\hat{z}$), the resulting force acts in the plane, causing electrons to undergo circular motion as seen below in Figure 15.

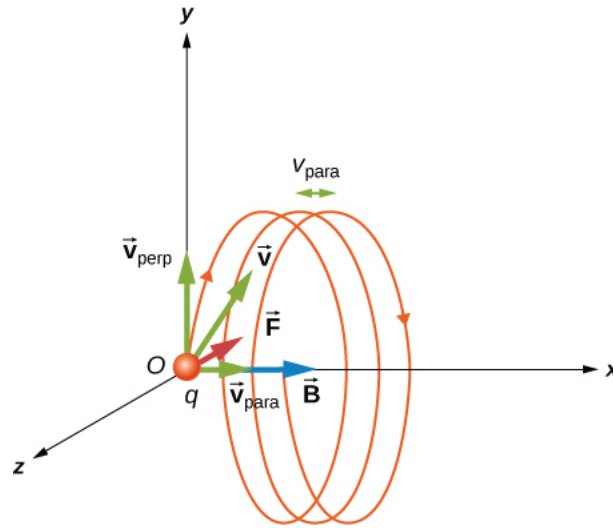


Figure 15: Cyclotron motion of a charged particle in a uniform magnetic field \mathbf{B} . The magnetic field is directed along the x -axis, and the particle (charge q) moves with a velocity \mathbf{v} , which can be decomposed into components parallel (\mathbf{v}_{para}) and perpendicular (\mathbf{v}_{\perp}) to the magnetic field. The Lorentz force $\mathbf{F} = q\mathbf{v} \times \mathbf{B}$ acts perpendicular to both \mathbf{v}_{\perp} and \mathbf{B} , causing circular motion in the y - z plane while allowing free motion along x , resulting in a helical trajectory [25]

Balancing this Lorentz force with the centripetal force gives:

$$\frac{mv^2}{r_c} = evB \quad (23)$$

Solving for the cyclotron radius r_c and the angular cyclotron frequency ω_c :

$$r_c = \frac{mv}{eB}, \quad \omega_c = \frac{v}{r_c} = \frac{eB}{m} \quad (24)$$

This orbital motion is called *cyclotron motion*, and the frequency ω_c sets the characteristic energy spacing for magnetic quantisation. In the simulations that follow, this term will be used to vary the strength of the perpendicular magnetic field.

Landau Quantisation and Magnetic Length

In quantum mechanics, the classical orbits become quantised into discrete energy levels called *Landau levels*, given by:

$$E_n = \hbar\omega_c \left(n + \frac{1}{2} \right), \quad n = 0, 1, 2, \dots \quad (25)$$

Each Landau level is highly degenerate and corresponds to an allowed quantised cyclotron orbit. As the magnetic field increases, so does the spacing between levels, enhancing quantum confinement.

The spatial extent of each Landau orbit is described by the *magnetic length* ℓ_B , defined as:

$$\ell_B = \sqrt{\frac{\hbar}{eB}} \quad (26)$$

This sets the scale over which the electron's wavefunction is localised in the presence of the magnetic field. Stronger fields lead to smaller ℓ_B , i.e., tighter confinement.

Simulating the Effect in a Saddle Potential

To model this effect, the simulation varies the cyclotron frequency ω_c , expressed as a ratio ω_c/ω_x , where ω_x is the curvature of the saddle potential in the transport direction.

Two energy scales are defined:

$$E_1 = \frac{\hbar\omega_x\omega_y}{2\omega_c} \quad (27)$$

$$E_2 = \hbar\omega_c \quad (28)$$

These determine the mode spacing and the width of the transition region. The Landau level energy for mode n is given by:

$$E_n = E_2 \left(n + \frac{1}{2} \right) \quad (29)$$

The transmission probability through the potential barrier is modelled using:

$$T_n = \frac{1}{1 + \exp(-\pi\epsilon_n)}, \quad \epsilon_n = \frac{E - E_n - V_0}{E_1} \quad (30)$$

The total conductance is then computed by summing over all modes:

$$G = \sum_n T_n \frac{e^2}{h}$$

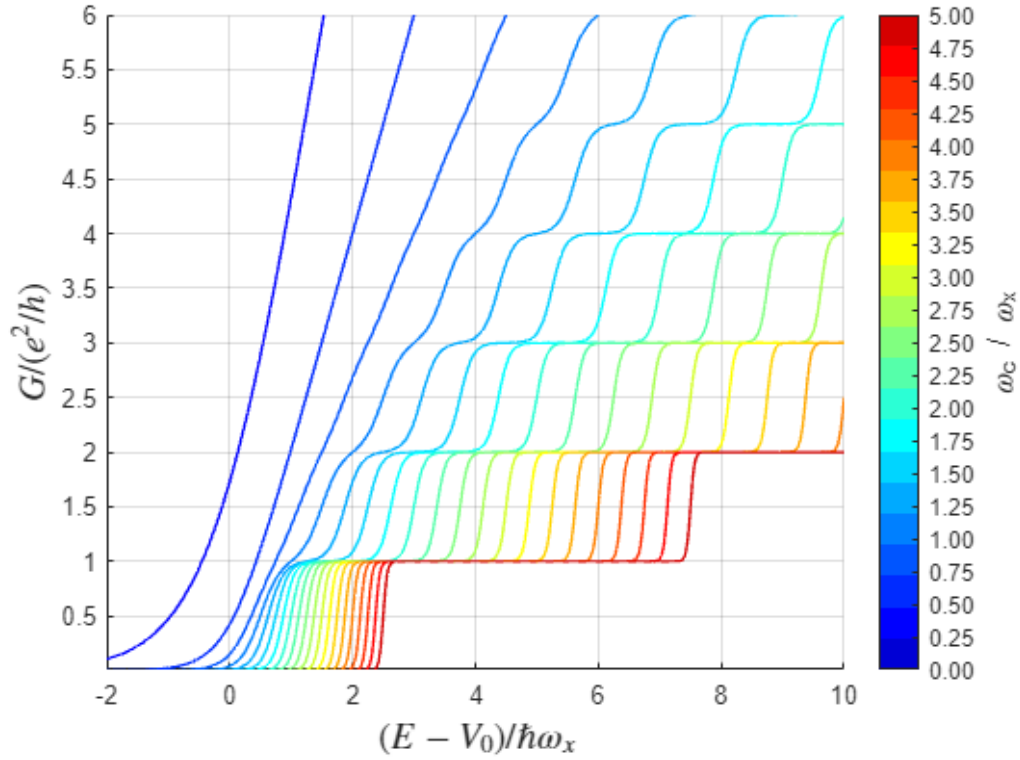


Figure 16: Simulated quantised conductance in the presence of a perpendicular magnetic field, shown as a function of scaled energy $(E - V_0)/\hbar\omega_x$ for increasing values of the cyclotron frequency ω_c , normalised to ω_x . The colour map represents different values of ω_c/ω_x , ranging from 0 (blue) to 5 (red) (Appendix 8.10)

After performing the simulation, it is observed that as ω_c increases, the conductance steps become noticeably sharper, more regularly spaced (i.e., plateaus are wider), and extend to higher quantised values. This marks a transition from a regime dominated by the saddle-point potential to one where Landau quantisation governs the transport behaviour. The introduction of a perpendicular magnetic field leads to the formation of discrete Landau levels, which enhances mode separation, reduces overlap between adjacent transmission functions, and produces well-defined conductance plateaus. In addition to improving the clarity of quantisation, magnetic confinement also enhances the overall stability of the system, as conductance becomes less sensitive to small variations in energy or gate voltage. These results demonstrate that another avenue of stabilising electron transport in low-dimensional systems is by introducing a perpendicular magnetic field.

3.6 Impact of Semiconductor Properties on Quantum Transport

In low-dimensional systems such as quantum point contacts, the intrinsic properties of the material have a profound effect on quantised conductance. Specifically, the *effective mass* m^* and the *Landé g -factor* are critical parameters that govern how electrons respond to confinement and external magnetic fields. The effective mass m^* appears in the Schrödinger equation and directly influences the kinetic energy term as well as the spacing between transverse subbands. A smaller effective mass leads to stronger quantum confinement, resulting in wider energy separation between modes, sharper conductance plateaus, and earlier onset of quantisation with respect to energy. Conversely, heavier effective masses produce more closely spaced subbands, which can reduce the clarity of quantisation and increase mode mixing.

The Landé g -factor determines the strength of spin splitting under an applied magnetic field via the Zeeman effect. Materials with large (or highly negative) g -factors exhibit greater spin splitting for the same magnetic field strength, resulting in more pronounced lifting of spin degeneracy. This alters the conductance staircase by introducing smaller, evenly spaced steps of e^2/h rather than $2e^2/h$, especially in the presence of an in-plane magnetic field. The choice of material therefore not only influences the energy scales of confinement and transport, but also determines the visibility and resolution of spin-resolved features in the conductance trace.

Effective Mass and Its Impact on Subband Structure

The effective mass is a measure of how the electron behaves under applied forces inside the crystal lattice, modifying both its kinetic energy and the curvature of the confinement potential. A smaller m^* results in a steeper potential and larger energy separation between transverse modes, leading to more distinct conductance steps.

In the simulation, the effective mass directly affects the Bohr magneton:

$$\mu_B = \frac{e\hbar}{2m^*} \quad (31)$$

This modifies the Zeeman energy splitting even when the g -factor and magnetic field are held constant:

$$E_{\text{Zeeman}} = \pm \frac{1}{2} g \mu_B B \quad (32)$$

The total energy for each subband becomes:

$$E_{n,s} = V_0 + \hbar\omega_y \left(n + \frac{1}{2} \right) + E_{\text{Zeeman}} \quad (33)$$

The transmission probability, scaled energy, and total conductance are computed in the same manner as in the previous sections, using the following expressions:

$$\begin{aligned} T_{n,s} &= \frac{1}{1 + \exp(-\pi\epsilon_n)}, \\ \epsilon_n &= \frac{E - E_{n,s}}{\hbar\omega_x}, \\ G &= \sum_{n,s} T_{n,s} \cdot \frac{e^2}{h} \end{aligned}$$

Material	Effective Mass (m^*)
Si (electrons)	$0.190 m_e$
InSb (electrons)	$0.013 m_e$
InGaAs (electrons)	$0.041 m_e$
GaAs (electrons)	$0.067 m_e$
GaAs (holes)	$0.500 m_e$

Table 1: Effective mass values used in the simulation for different semiconductor materials, including both electron and hole configurations

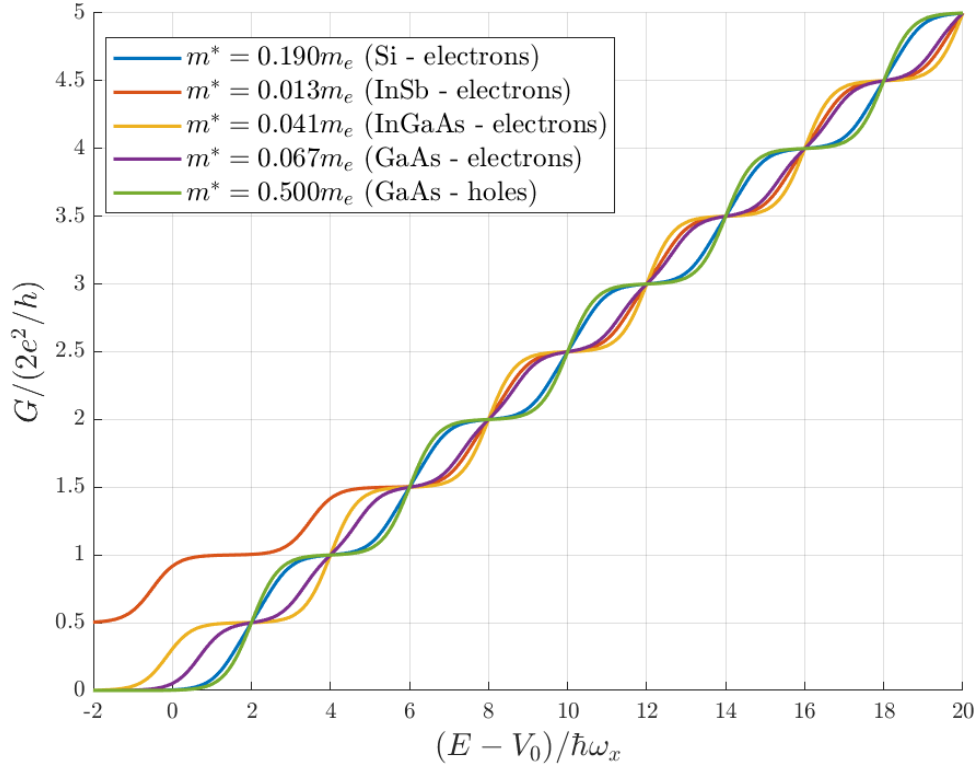


Figure 17: Simulated quantised conductance for different effective masses: InSb ($m^* = 0.013m_e$), GaAs ($m^* = 0.067m_e$), and Si ($m^* = 0.19m_e$) under a fixed magnetic field of 10 T and a confinement ratio of $\omega_y/\omega_x = 4$. Lighter effective masses lead to sharper and earlier-onset conductance plateaus due to stronger confinement and larger Zeeman splitting (Appendix 8.11)

Figure 17 illustrates how the quantised conductance of a quantum point contact varies for different effective masses m^* , showcasing both electrons and holes in semiconductors such as Si, InSb, InGaAs, and GaAs. A general trend can be observed: materials with smaller effective masses (e.g., InSb electrons, $m^* = 0.013 m_e$) exhibit earlier onset of conductance and sharper plateaus, while those with larger effective masses (e.g., GaAs holes, $m^* = 0.500 m_e$) show a delayed onset and smoother transitions.

The effective mass influences both the Bohr magneton, $\mu_B \propto 1/m^*$, and the curvature of the potential via the confinement frequency ω_y , thereby modifying the spacing between quantised modes. Lighter particles experience tighter confinement and hence larger sub-band spacing, allowing distinct conductance steps to appear more readily.

The appearance of $0.5 \times (2e^2/h) = e^2/h$ steps at low energies in some materials (e.g., InSb) indicates strong Zeeman spin splitting, often seen in materials with high g -factors or low m^* , where spin degeneracy is lifted. In contrast, systems with heavier carriers or negligible g -factors maintain spin-degenerate modes, leading to conductance increasing in full $2e^2/h$ steps.

Additionally, holes (as in GaAs) generally have higher effective masses and may show more gradual conductance onset due to smaller subband spacing and less pronounced Zeeman effects. The result is a set of conductance curves where material-specific parameters — particularly m^* and spin properties — shape the visibility, spacing, and resolution of the quantised plateaus. This highlights how intrinsic semiconductor properties critically influence quantum transport characteristics in low-dimensional systems.

Landé g -Factor and Spin Splitting

The Landé g -factor describes how strongly the electron's spin couples to an external magnetic field, directly influencing the size of the Zeeman splitting:

$$\Delta E_Z = g\mu_B B \quad (34)$$

Material	g -Factor
Si	2.0
Ge	1.6
GaAs	-0.4
InAs	-14.0
InGaAs	-4.5
InSb	-51

Table 2: g -factor values used in the simulation for various bulk semiconductors.

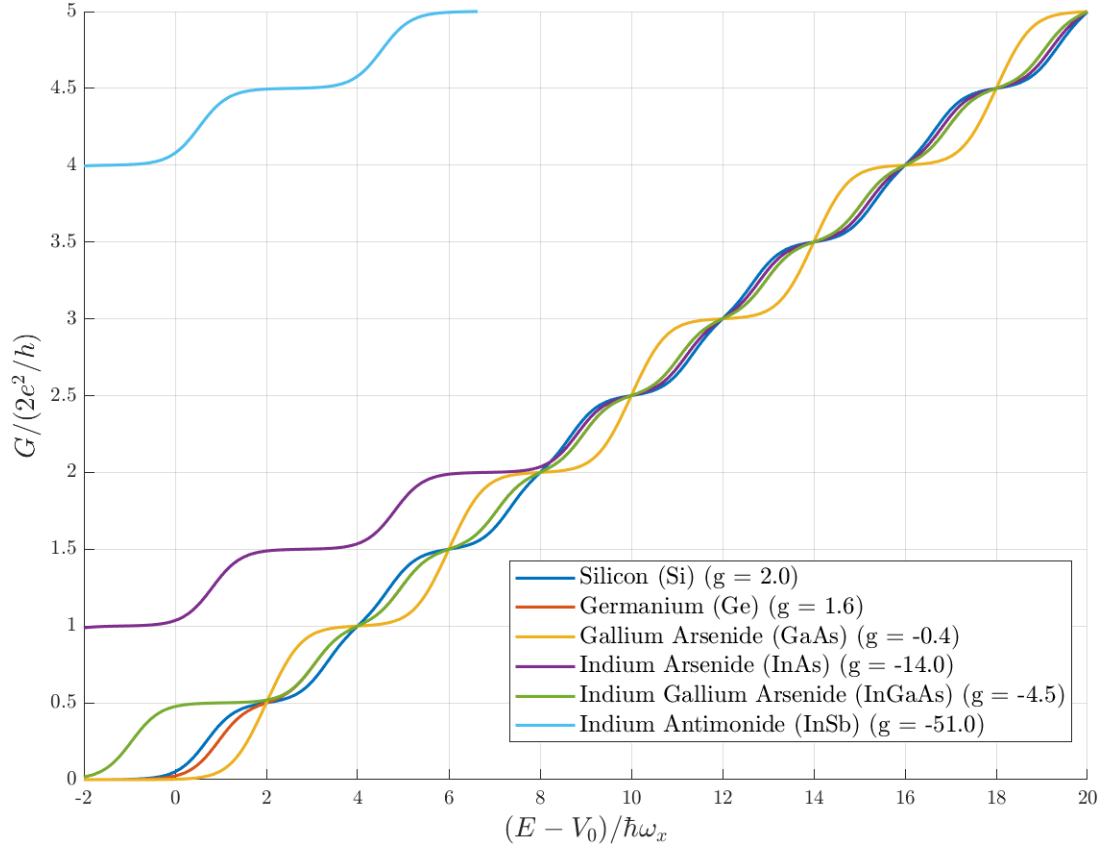


Figure 18: Simulated quantised conductance for different bulk semiconductors under a fixed magnetic field of 10 T (Appendix 8.12)

Figure 18 illustrates the impact of material-specific g -factors on the quantised conductance of quantum point contacts in the presence of an in-plane magnetic field. Each curve corresponds to a different bulk semiconductor, with g -factors ranging from small values (e.g., $g = 2.0$ for Si and $g = 1.6$ for Ge) to highly negative values (e.g., $g = -14.0$ for InAs and $g = -51.0$ for InSb).

Most materials exhibit conductance quantisation in steps of approximately e^2/h , indicating that spin degeneracy is lifted by the applied magnetic field. This includes materials with both small and large g -factors, such as Si, Ge, InAs, InGaAs, and InSb, where the spin-split subbands contribute individually to transport. The spacing between steps reflects the degree of Zeeman splitting, which is proportional to the Landé g -factor.

In contrast, GaAs—having a small and negative g -factor ($g = -0.4$)—exhibits conductance steps closer to $2e^2/h$, suggesting that spin degeneracy remains largely intact under the same magnetic field conditions. This leads to fewer, broader plateaus in the staircase.

Notably, materials with larger $|g|$ values, such as InAs and especially InSb ($g = -51$), show highly resolved spin-split conductance steps. For InSb, the conductance begins at $4e^2/h$, revealing that multiple spin-resolved modes are already conducting at low energies. This highlights the strong influence of the g -factor on transport properties in quantum point contacts under magnetic fields.

These results confirm that materials with higher $|g|$ undergo more significant Zeeman splitting and therefore display finer spin-resolved quantisation. This tunability is essential for applications in spintronics and quantum information, where control over individual spin channels is critical.

Carrier-Type Dependence in GaAs.

The comparison was extended to electrons and holes in GaAs as focused in this report, where the electron g -factor is small and negative ($g = -0.4$), while the hole g -factor is significantly larger and positive ($g \approx 3.6$). The resulting spin splitting for holes is more prominent, producing more widely spaced conductance plateaus.

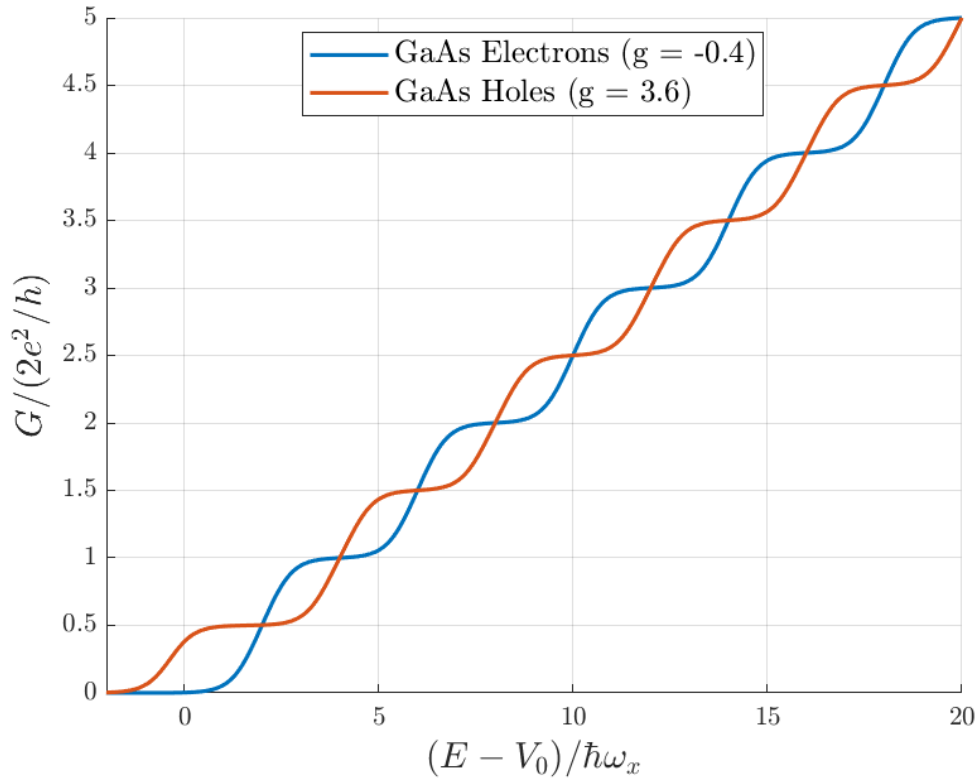


Figure 19: Comparison of quantised conductance in GaAs for electrons ($g = -0.4$) and holes ($g \approx 3.6$). The hole trace exhibits significantly greater spin splitting and more widely spaced conductance steps under the same magnetic field (10 T), highlighting the role of carrier type and band structure (Appendix 8.13)

Figure 19 compares the quantised conductance of electrons and holes in GaAs, highlighting the effect of their distinct Landé g -factors. GaAs electrons have a small negative g -factor ($g = -0.4$), resulting in minimal Zeeman splitting under an applied magnetic field. Consequently, their conductance staircase retains relatively uniform steps, close to $2e^2/h$. In contrast, GaAs holes exhibit a much larger g -factor ($g = 3.6$), which leads to stronger spin splitting. This is reflected in the smoother and more densely spaced conductance steps observed in the hole trace, particularly at low energies. These results demonstrate how the sign and magnitude of the g -factor significantly influence spin-resolved transport properties, even within the same material system.

3.7 Temperature Dependence of Quantised Conductance

To investigate the impact of temperature on quantised conductance, a simulation was developed to calculate the conductance through a quantum point contact as a function of scaled energy for a range of temperatures. The theoretical foundation for this analysis is provided by the Landauer-Büttiker formalism [26], which relates conductance to the energy-dependent transmission probability and the thermal distribution of electrons:

$$G(T) = \frac{2e^2}{h} \int T(E) \left(-\frac{\partial f(E, T)}{\partial E} \right) dE, \quad (35)$$

where $T(E)$ is the transmission probability and $f(E, T)$ is the Fermi-Dirac distribution. At absolute zero, the derivative $-\partial f/\partial E$ becomes a Dirac delta function centred at the Fermi energy, and conductance steps are ideally sharp. At finite temperatures, however, this derivative broadens over an energy window of approximately $\sim k_B T$, resulting in smearing of the steps due to thermal excitation of electrons into higher energy subbands.

The simulation uses a discrete summation of the Landauer formula [26], expressed as:

$$G = \frac{1}{2e^2/h} \sum_n T_n(E) \cdot f(E_n - E), \quad (36)$$

where $T_n(E)$ is the transmission probability for the n -th subband, and $f(E_n - E)$ is the Fermi-Dirac distribution shown in Figure 20:

$$f(E) = \frac{1}{1 + \exp\left(\frac{E}{k_B T}\right)}. \quad (37)$$

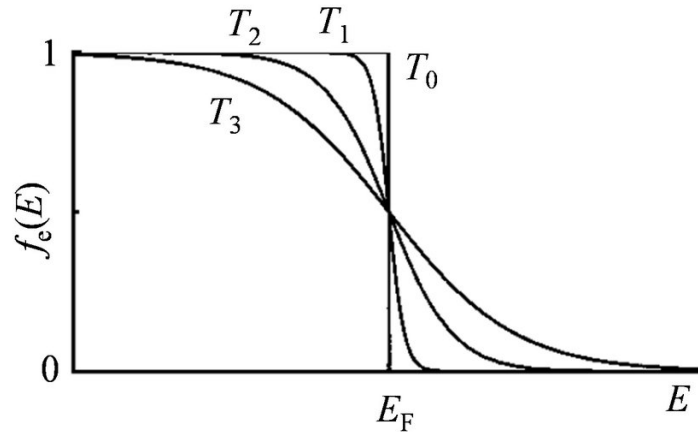


Figure 20: Effect of temperature on the Fermi-Dirac distribution $f(E)$. The horizontal axis represents the electron energy E , while the vertical axis shows the probability $f(E)$ that a state at energy E is occupied. The curves correspond to increasing temperatures with $T_3 > T_2 > T_1 > T_0$, showing how the distribution broadens as temperature increases

The transmission probability for each subband is defined using a smoothed step-like function:

$$T_n(E) = \frac{1}{1 + \exp(-\pi\epsilon_n)}, \quad \epsilon_n = \frac{E - E_n}{\hbar\omega_x}. \quad (38)$$

At zero temperature ($T = 0$ K), the Fermi-Dirac distribution becomes a perfect step function, meaning that all electron states below the Fermi energy E_F are fully occupied, while those above are completely empty. This results in a sharp occupation profile and ensures that only subbands with $E_n < E_F$ contribute to conductance. Consequently, the conductance exhibits distinct, sharp steps at integer multiples of $2e^2/h$.

However, as temperature increases (e.g., T_1 to T_3), thermal excitation allows electrons to occupy states above the Fermi level while some states below E_F become depopulated. This broadens the transition between occupied and unoccupied states over an energy range on the order of $\sim k_B T$, a phenomenon known as thermal broadening. As a result, the previously sharp Fermi step becomes more gradual, reducing the contrast between conductance plateaus and transitions.

As shown in Figure 22 below, this broadening leads to smoother transitions between conductance steps. Electrons begin to populate higher-energy subbands prematurely, causing the conductance to rise more gradually instead of exhibiting discrete jumps.

At elevated temperatures ($T \geq 10$ K), this effect becomes even more pronounced. The quantised nature of conductance becomes increasingly obscured, particularly in higher-energy modes where subband spacings in Figure 21 shown below are narrower. The staircase profile effectively transforms into a smooth curve, indicating a degradation of quantisation due to thermal effects. This is most evident in the extreme case of $T = 50$ K, included in Figure 22 for illustrative purposes, where the conductance trace shows a near-complete loss of discrete plateaus.

This highlights how thermal excitation overwhelms the confinement-induced energy structure at sufficiently high temperatures. These results underscore the importance of cryogenic operating conditions in experiments aiming to observe and utilise well-defined quantised conductance features.

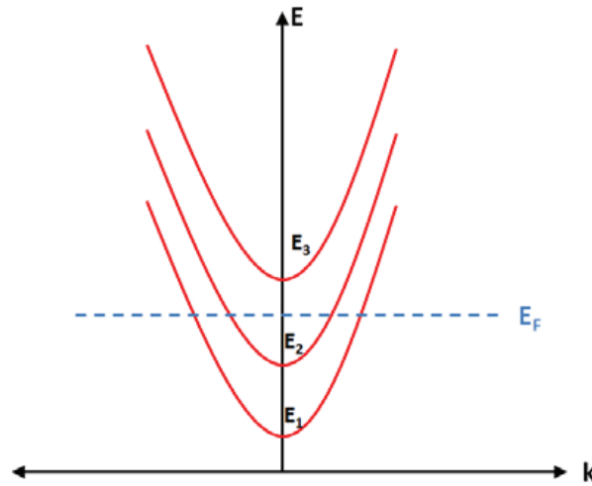


Figure 21: Energy dispersion of quantised subbands in a quasi-one-dimensional channel. Each parabola represents a transverse mode (or subband), with energies E_1 , E_2 , and E_3 corresponding to the quantised levels due to lateral confinement [27]

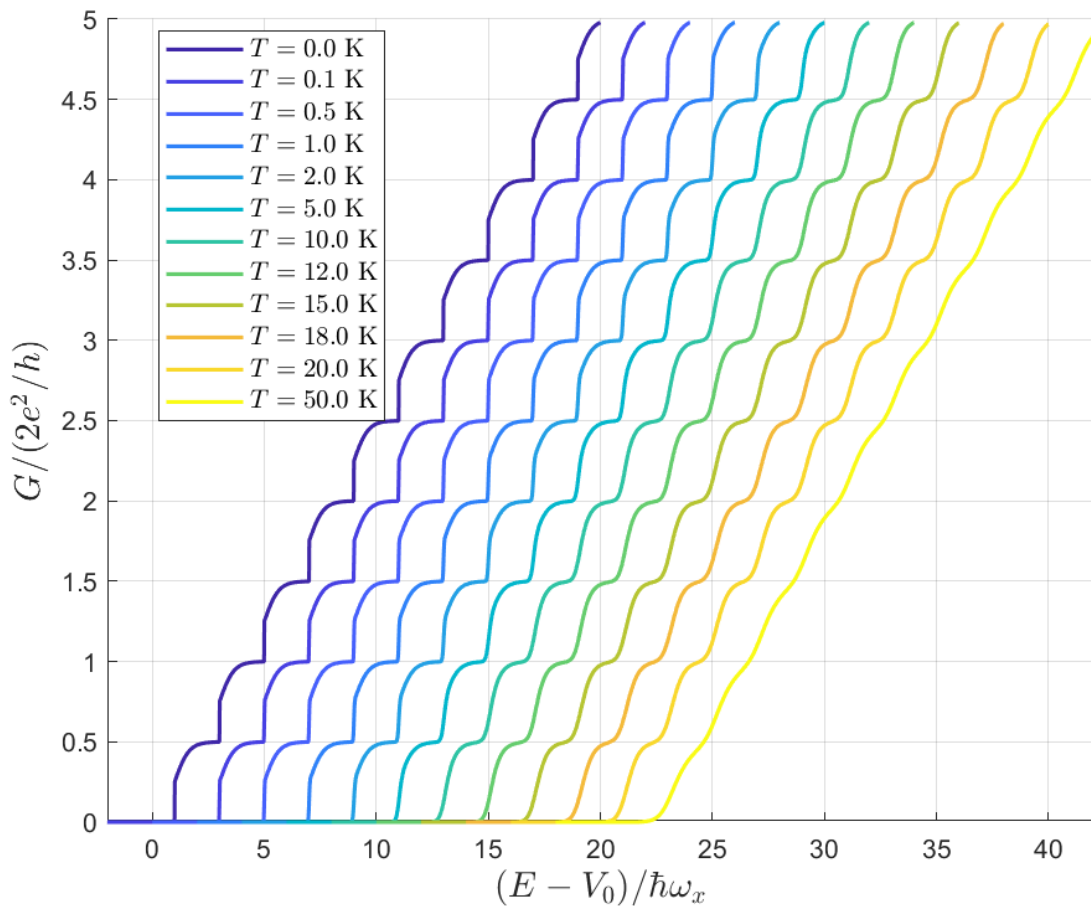


Figure 22: Simulated quantised conductance curves at different temperatures, plotted against scaled energy $(E - V_0)/\hbar\omega_x$. Horizontal offsets have been added for clarity. As temperature increases, thermal broadening leads to smoother transitions between conductance plateaus. At high temperatures, quantisation features become increasingly suppressed (Appendix 8.14)

These results highlight how the interplay between transmission probability and thermal occupancy governs the behaviour of quantised conductance. Understanding this relationship is essential for interpreting experimental data and for designing quantum point contacts that preserve quantisation fidelity across a range of operating temperatures.

While simulations often assume an idealised zero-temperature limit ($T = 0\text{ K}$)—which yields perfectly sharp conductance steps—this condition is physically unattainable in practice. However, experimentally achievable cryogenic temperatures such as $T = 100\text{ mK}$ are sufficiently low that they reproduce similar characteristics. At these temperatures, the Fermi-Dirac distribution remains sharply defined near the Fermi level, resulting in conductance traces that closely resemble the theoretical step-like behaviour, with only minor rounding at the transitions.

This theoretical expectation is confirmed by our simulation results, which show well-defined plateaus at $T = 0\text{ K}$ and similarly sharp features at $T = 100\text{ mK}$. As temperature increases, the expected smoothing of the conductance steps due to thermal broadening becomes clearly visible, validating the predicted influence of the Fermi-Dirac distribution on quantised transport.

4 Results Analysis & Discussion

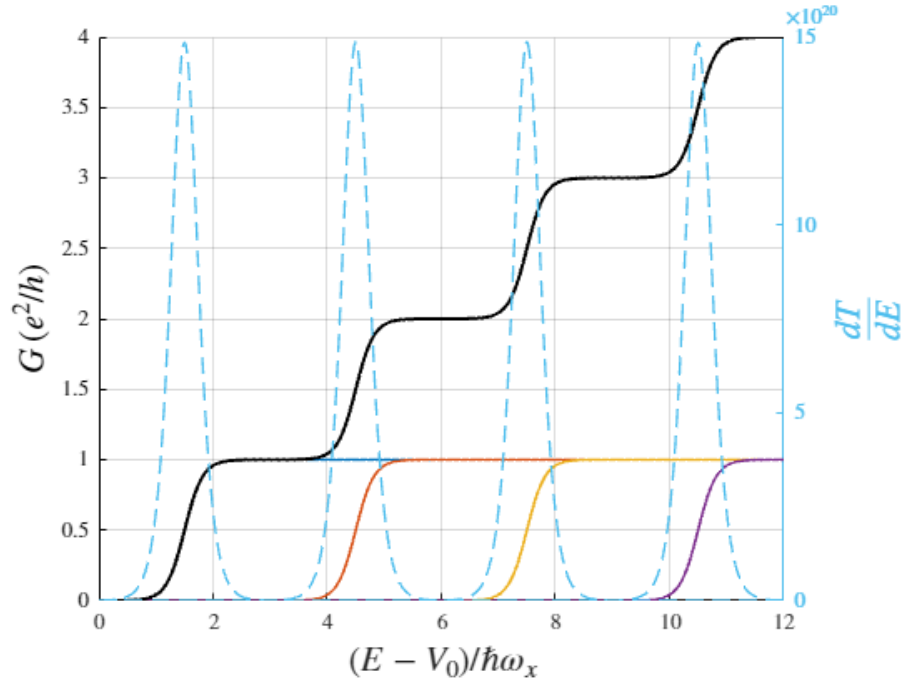


Figure 23: Overlay of quantised conductance G (black) and the transmission derivative with respect to energy $\frac{dT}{dE}$ (blue dashed). Each peak in $\frac{dT}{dE}$ corresponds to the energy threshold where a new subband begins to conduct, marking a critical transition point in the staircase structure. Flat conductance plateaus are reflected as troughs in the derivative, indicating regions of maximal stability and fully open transmission channels (Appendix 8.15)

Figure 23 overlays the quantised conductance trace (black curve) with the transmission derivative with respect to energy $\frac{dT}{dE}$ (blue dashed curve), offering insight into the dynamics of mode activation in the quantum point contact. Each peak in $\frac{dT}{dE}$ corresponds to a point of rapid change in the transmission probability of a given mode, precisely where a new subband begins to contribute to conductance. These peaks mark the critical energy thresholds where the transverse mode transitions from being closed to partially open, indicating the most energy-sensitive regions of the device.

Troughs in $\frac{dT}{dE}$, where the derivative approaches zero, align with the flat regions of the conductance staircase—the quantised plateaus. In these regions, transmission probabilities remain nearly constant and equal to 1, indicating fully open modes with minimal sensitivity to changes in Fermi energy. Thus, the transmission derivative acts as a diagnostic tool, highlighting energy intervals where the QPC is most responsive to external tuning (e.g., via gate voltage or temperature).

4.1 Further Analysis into Confinement Ratio Relationship

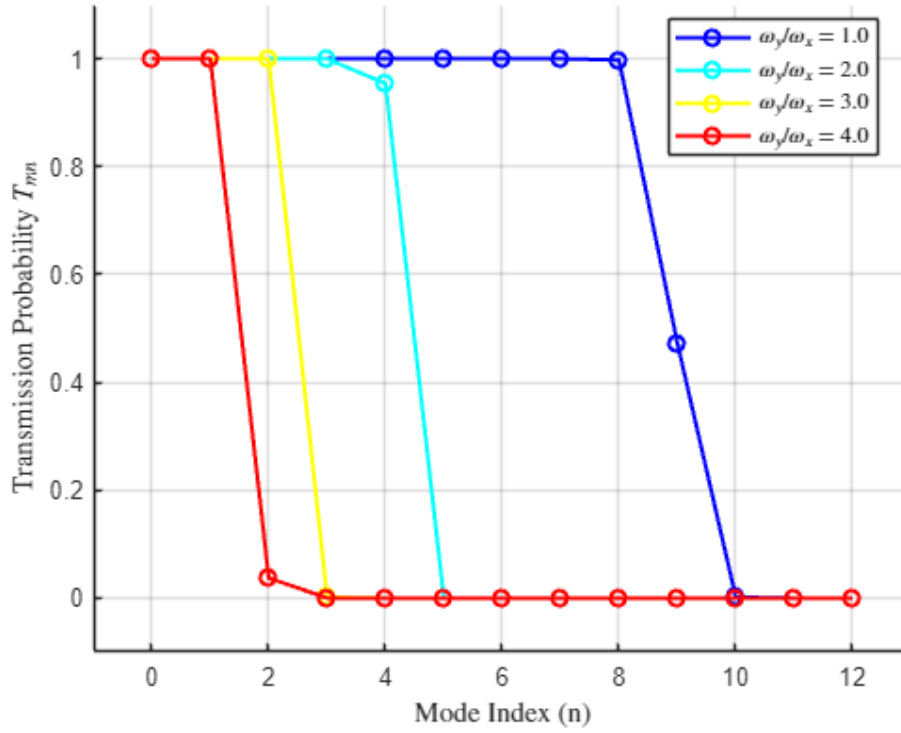
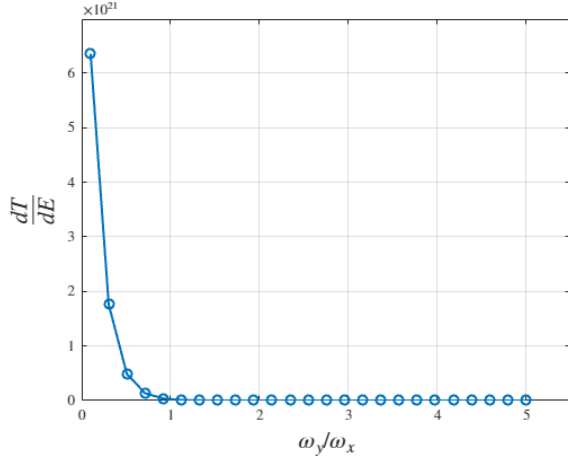
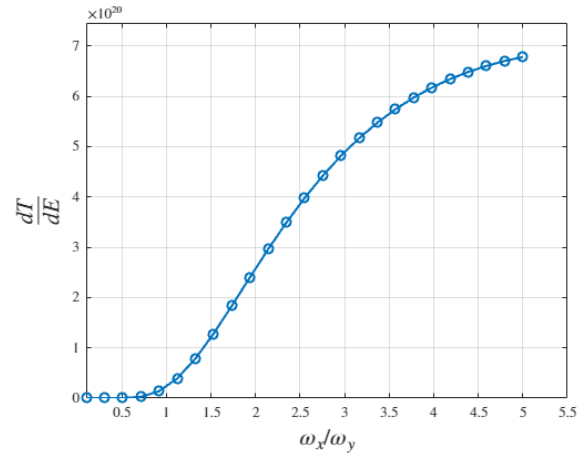


Figure 24: Simulated transmission probabilities T_n for different confinement ratios ω_y/ω_x . As the ratio increases from 1.0 to 4.0, the number of modes with high transmission decreases sharply. This indicates that stronger transverse confinement effectively limits the number of energetically accessible channels, enhancing mode selectivity and improving conductance quantisation (Appendix 8.16)

Figure 24 reinforces the role of the confinement ratio in shaping transport characteristics. As ω_y/ω_x increases, only the lowest few modes remain energetically and spatially accessible. Higher modes experience reduced transmission due to the stronger lateral confinement, which raises their subband thresholds beyond the Fermi energy. This suppression of higher-order modes leads to cleaner, more well-defined conductance steps, and highlights the importance of engineering the confinement profile to control the number of transmitting channels in quantum point contacts.



(a) Transmission derivative vs ω_y/ω_x



(b) Transmission derivative vs ω_x/ω_y

Figure 25: Variation of the transmission derivative $\frac{dT}{dE}$ with confinement ratios. A high ω_y/ω_x (left) leads to sharper quantisation steps and greater stability, while increasing ω_x/ω_y (right) results in steeper transitions and more energy sensitivity (Appendix 8.17)

To quantitatively assess the sharpness of conductance steps, the derivative of the transmission probability with respect to energy, $\frac{dT}{dE}$, was evaluated as a function of the confinement ratios. As shown in Figure 25, the left plot reveals that increasing ω_y/ω_x —which corresponds to stronger transverse confinement—results in a rapid decrease in $\frac{dT}{dE}$. This indicates a flattening of the transmission function, leading to broader conductance plateaus and enhanced system stability. In contrast, the right plot demonstrates that increasing ω_x/ω_y , representing steeper longitudinal confinement, causes a significant rise in the transmission derivative. This steeper energy dependence leads to more abrupt transitions between conductance plateaus, which may result in increased sensitivity to energy fluctuations and reduced quantisation clarity.

4.2 Differential Conductance under Varying In-Plane Magnetic Fields

To gain deeper insight into the energy-dependent transport behaviour in the presence of an in-plane magnetic field, the quantised conductance curves were transformed into a differential conductance map by numerically evaluating the derivative of conductance with respect to energy, $\frac{dG}{dE}$. This technique enhances the visibility of transition regions between plateaus, highlighting areas where conductance changes most rapidly.

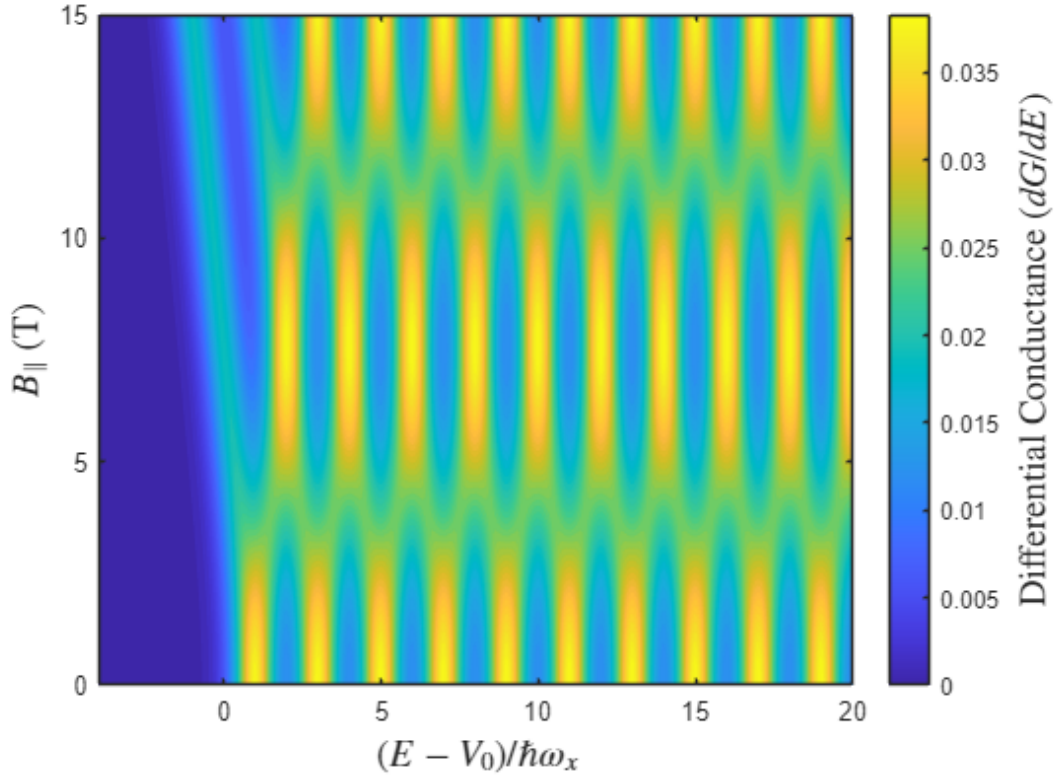


Figure 26: Differential conductance map showing $\frac{dG}{dE}$ as a function of scaled energy $(E - V_0)/\hbar\omega_x$ and in-plane magnetic field $B_{||}$. Dark blue regions correspond to flat conductance plateaus where $\frac{dG}{dE} \approx 0$, while bright yellow bands highlight energy regions where new spin-resolved modes begin conducting. Green areas represent smooth transitions between steps (Appendix 8.18)

Figure 26 displays the differential conductance as a function of scaled energy $(E - V_0)/\hbar\omega_x$ and magnetic field strength $B_{||}$. In this colour map, dark blue regions indicate $\frac{dG}{dE} \approx 0$, corresponding to flat conductance plateaus where the system exhibits minimal sensitivity to energy variation—signifying transport through fully open modes. Bright yellow bands mark peaks in $\frac{dG}{dE}$, which represent the energy positions where new 1D sub-bands begin contributing to conductance and where rapid transitions between plateaus occur. Green regions capture the intermediate transitions between plateau and step.

Importantly, as the magnetic field increases, spin degeneracy is lifted and the conductance steps split into finer increments of e^2/h , as previously shown. In this map, these spin-split transitions appear as alternating peaks that shift with increasing field, allowing for clear visual indexing of individual spin-resolved plateaus.

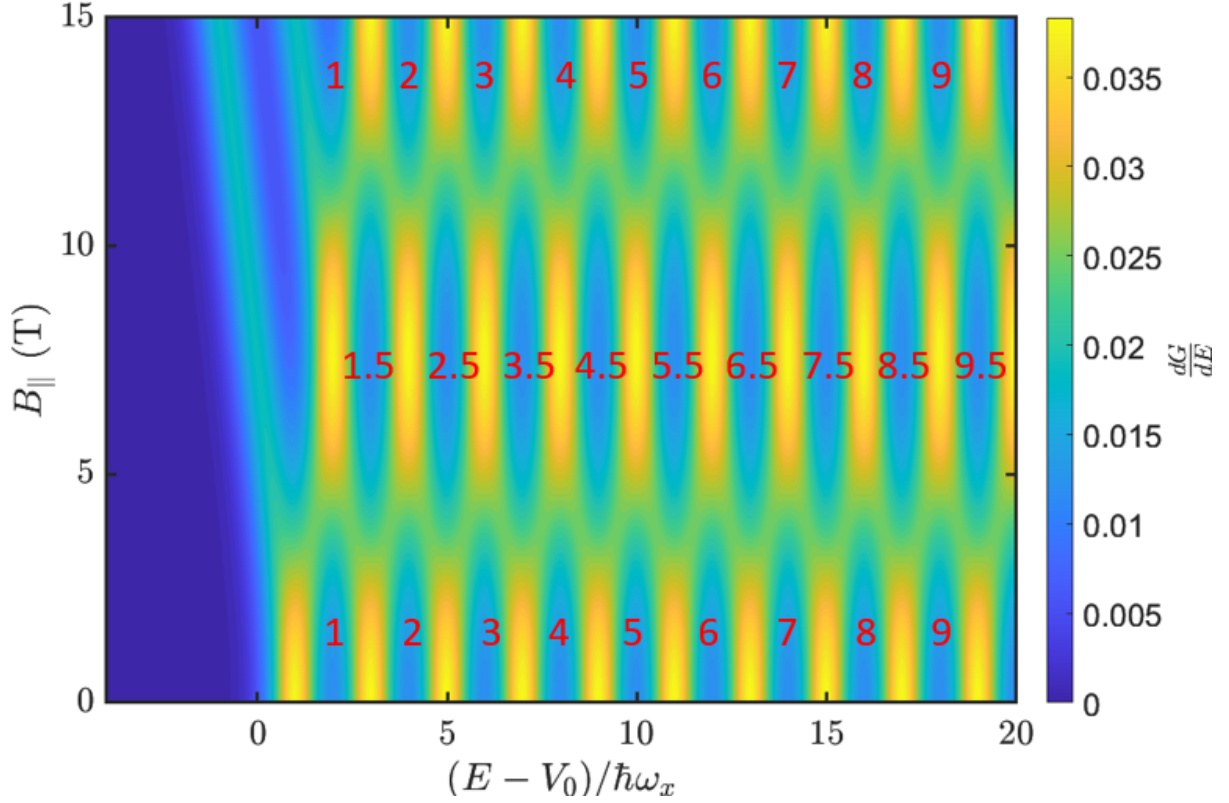


Figure 27: Indexed differential conductance map showing $\frac{dG}{dE}$ as a function of scaled energy $(E - V_0)/\hbar\omega_x$ and in-plane magnetic field B_{\parallel} . The red numerical labels indicate the quantised conductance plateaus, including both integer and spin-resolved half-integer values

The annotated differential conductance plot in Figure 27 provides a clear visualisation of spin-resolved conductance steps as the in-plane magnetic field B_{\parallel} is increased. Each peak in the differential conductance corresponds to a transition between quantised plateaus, and by numerically indexing these peaks, one can identify the emergence of both integer and half-integer plateaus. At zero field, conductance steps occur at $G = 1, 2, 3, \dots \times (2e^2/h)$, reflecting spin-degenerate transport. As B_{\parallel} increases, the Zeeman effect lifts this degeneracy, resulting in intermediate plateaus at half-integer multiples of $2e^2/h$, i.e., $G = 0.5, 1.5, 2.5, \dots \times (2e^2/h)$. These newly formed spin-resolved plateaus are indexed accordingly in red, allowing for the tracking of individual spin-split subbands.

The ability to resolve and index these features is crucial for understanding spin-polarised transport, and is especially relevant in spintronics and quantum information contexts, where precise control over spin channels is essential. This indexing not only confirms the theoretical expectations from Zeeman splitting but also demonstrates the utility of differential conductance maps in characterising spin-dependent quantisation in quantum point contacts.

4.3 Thermal Effects on Subband Activation and Conductance Sharpness

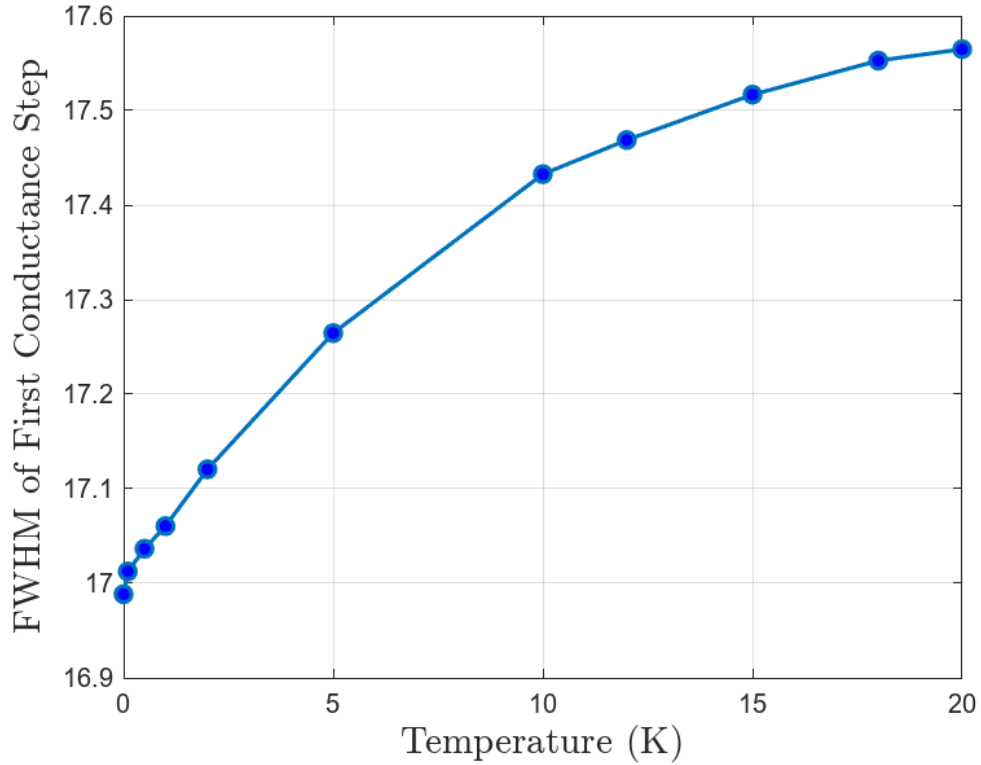


Figure 28: Full Width at Half Maximum (FWHM) of the first conductance step as a function of temperature. At low temperatures, the FWHM remains nearly constant, reflecting sharp transitions in the conductance curve. As temperature increases, thermal broadening smoothens the transition between conductance plateaus, leading to an increase in FWHM (Appendix 8.14)

The plot in Figure 28 illustrates how the full width at half maximum of the first quantised conductance step evolves with increasing temperature. The FWHM measures the energy range over which the conductance rises from its baseline to half of the first quantised value (i.e., from 0 to e^2/h), providing a quantitative indicator of how sharply defined the step is. A smaller FWHM corresponds to a steeper, more abrupt step—characteristic of low thermal broadening—while a larger FWHM indicates a smoother transition caused by increased thermal occupation of higher energy states.

At very low temperatures (below ~ 2 K), the FWHM remains nearly constant, reflecting the fact that the Fermi-Dirac distribution behaves almost like a step function and thermal energy $k_B T$ is negligible compared to subband spacing. In this regime, electrons populate subbands strictly below the Fermi level, and conductance transitions remain sharp. However, as temperature increases beyond this point, thermal broadening becomes significant. The thermal energy becomes comparable to the subband energy spacings, allowing electrons to partially occupy higher subbands even before the Fermi level reaches them. This smoothens the conductance step, as evidenced by the steady increase in FWHM.

The FWHM is calculated using $\text{FWHM} = E_{\text{max}} - E_{\text{min}}$, where E_{min} and E_{max} are the energy values at which the conductance first crosses the half-maximum threshold. The

upward trend in this plot supports the theoretical prediction that higher temperatures reduce quantisation sharpness and shift the system from well-defined steps to more continuous conductance transitions.

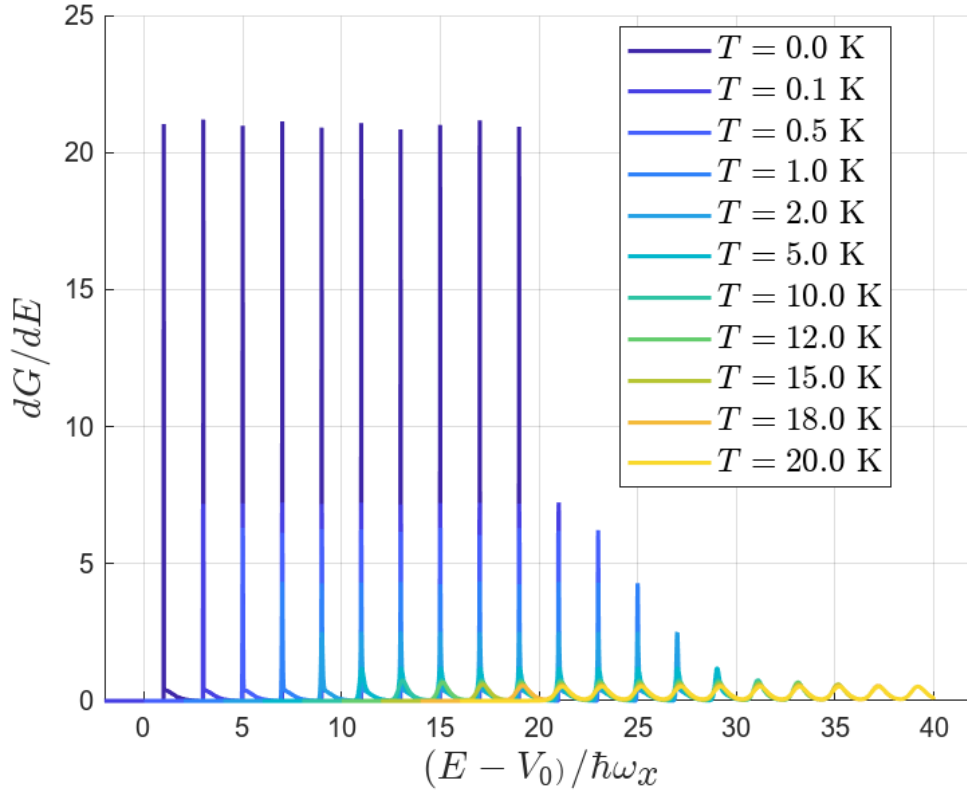


Figure 29: Differential conductance dG/dE plotted against scaled energy for a range of temperatures. At $T = 0$ K, sharp, high-amplitude peaks mark the onset of each conductance step. As temperature increases, thermal broadening causes these peaks to flatten and spread out, reflecting smoother transitions and reduced quantisation clarity (Appendix 8.14)

Figure 29 presents the differential conductance dG/dE as a function of scaled energy $(E - V_0)/\hbar\omega_x$ for various temperatures. The differential conductance quantifies how sharply the conductance changes with respect to energy and therefore serves as a useful tool for analysing the sharpness of conductance plateaus and transitions.

At $T = 0$ K, the derivative displays tall, narrow peaks that correspond to extremely sharp conductance steps. This is consistent with the Fermi-Dirac distribution behaving as a step function, where transitions between occupied and unoccupied states occur abruptly. Each peak aligns with the onset of a new conducting mode and reflects a clear transition between quantised levels.

As temperature increases, thermal broadening of the Fermi-Dirac distribution causes the derivative peaks to become shorter and wider. The sharpness of the conductance transitions is reduced, and the peaks spread over a broader energy range. This effect becomes noticeable around $T = 2$ K and increases steadily with temperature. At elevated temperatures ($T \geq 10$ K), the peaks are significantly diminished and flattened, indicating the near-complete loss of well-defined conductance plateaus. The derivative curves at these

temperatures reveal only weak oscillations in dG/dE , suggesting a smooth, rather than stepped, conductance profile.

This plot provides a visual confirmation of how thermal effects degrade quantised conductance. The loss of sharpness in the dG/dE peaks corresponds directly to the smearing of conductance steps, as electrons are thermally excited across subbands even before the Fermi level aligns with their threshold energies. The transition from narrow, delta-like peaks to broad, low-amplitude curves is a hallmark of temperature-induced degradation in quantum point contact behaviour.

5 Future Work

While this project has successfully demonstrated the behaviour of quantised conductance in a quantum point contact under various physical conditions, there remain numerous opportunities to expand the scope of the work both theoretically and practically. The MATLAB-based simulation framework developed here is modular and flexible, making it suitable for several extensions that would enhance realism, introduce more complex physics, and bridge the gap between theoretical predictions and experimental systems.

To enable more sophisticated simulations, a natural progression would be to transition to specialised quantum transport packages such as *Kwant*—a Python-based open-source software designed for tight-binding modelling of mesoscopic systems. Kwant supports arbitrary geometries, handles complex potential landscapes, and readily incorporates external fields, disorder, and magnetic flux. It also facilitates computation of scattering matrices, local densities of states, and current distributions, enabling deeper insight into spatially resolved transport properties. Importantly, Kwant can interface with other Python libraries such as NumPy and SciPy, allowing integration with self-consistent solvers or machine learning algorithms for parameter optimisation. By migrating the model to Kwant, future work could simulate real device geometries more accurately and explore phenomena beyond the reach of analytical or semi-classical approximations. *Kwant* is also widely adopted in current quantum transport research and has been featured in numerous peer-reviewed studies focusing on nanostructured devices, topological materials, and quantum Hall systems.

One natural direction for extension is the incorporation of more realistic electrostatic potentials [28]. The current model assumes an idealised saddle-point potential to approximate the constriction formed by surface gates. While this captures the essential physics, it omits several real-world features that emerge from practical device fabrication, including non-uniform gate geometries, fringe effects, and doping inhomogeneities. Future work could solve the Poisson equation self-consistently alongside the Schrödinger equation to obtain more accurate potential landscapes. Finite element methods or analytical techniques using real gate geometries would enable the simulation of more realistic confinement profiles and help quantify the role of device imperfections on quantised conductance.

Another promising area of development is non-equilibrium transport [29]. The present analysis assumes linear response conditions, i.e., infinitesimally small source-drain bias. However, many experimental setups involve finite voltage drops across the QPC. Including finite-bias effects in the Landauer-Büttiker framework would allow for the study of non-linear conductance, energy-resolved subband population, and heating effects. These are particularly important for investigating current saturation, rectification, and quantum pumping mechanisms.

Furthermore, the model could be extended to the time-dependent regime. Time-dependent gate voltages lead to phenomena such as photon-assisted tunnelling and dynamical modulation of transmission channels. This would require solving the time-dependent Schrödinger equation to capture periodic driving. Such studies are relevant in the design of quantum electron pumps, single-electron sources, and high-speed quantum logic operations.

In addition, the influence of disorder and impurity scattering could be explored [30]. Real QPCs exhibit residual disorder due to ionised dopants, surface roughness, and fabrication imperfections. Simulating conductance in the presence of random potential fluctuations would allow analysis of robustness to imperfections and the emergence of mesoscopic phenomena such as universal conductance fluctuations and weak localisation.

Another direction is to apply the model to alternative material platforms [31]. While GaAs/AlGaAs was used in this work due to its favourable band structure and fabrication maturity, emerging materials such as graphene, transition metal dichalcogenides (TMDs), and topological insulators offer unique transport characteristics. These include linear dispersion, spin-valley coupling, and topologically protected edge states. Adapting the simulation to capture the physics of these materials—by modifying the band structure—would greatly enhance the scope and modern relevance of the tool.

Spin-orbit coupling (SOC) could also be introduced into the simulation [32]. Both Rashba and Dresselhaus SOC terms are particularly relevant in low-dimensional systems and play key roles in spintronic and quantum computing applications. Including SOC would allow the investigation of spin-precession, spin filtering, and electrically controlled spin-splitting, even in the absence of magnetic fields. Coupled with an external field, this could reveal spin-orbit-induced spin textures and novel spin-polarised transport regimes.

Future work could also focus on benchmarking the simulation against experimental data. While this report has validated its results against theoretical expectations, parameter fitting to real measurements from literature or laboratory experiments would provide more robust validation. This would enable extraction of quantities such as the effective mass, g-factor, and potential profile from data, and improve the model’s predictive capabilities.

From a quantum information perspective, QPCs are used in qubit architectures for spin readout and charge sensing. In such systems, the QPC operates as an electrometer sensitive to single-electron transitions in adjacent quantum dots. Modelling this capacitive coupling and simulating QPC back-action, signal-to-noise ratio, and readout fidelity would be highly valuable for qubit design and scalable quantum processors to explore further how it would be applied to the industry.

In summary, the current simulation provides a robust framework for studying quantised conductance in QPCs under a variety of conditions. However, its versatility allows for many valuable extensions: incorporating realistic electrostatics, finite bias, and time dependence; including interactions and disorder; exploring novel materials and spin effects; benchmarking with experiment; and improving usability. Each of these directions would help align the simulation more closely with state-of-the-art quantum transport research, and contribute to the design of next-generation low-dimensional electronic and quantum devices.

6 Conclusion

This project has successfully demonstrated the core principles of quantised conductance in quantum point contacts using a combination of theoretical analysis and MATLAB-based simulations. By systematically investigating how various physical parameters—such as confinement strength, magnetic field orientation, material properties, and temperature—affect conductance behaviour, this work provides a comprehensive picture of one-dimensional (1D) electron transport in mesoscopic systems.

The foundational framework of this study is the Landauer-Büttiker formalism, which connects the quantum conductance of a device to the transmission probabilities of its available modes. Starting from this formalism, the project implemented a detailed simulation pipeline that captures the conductance response as a function of scaled energy, allowing for meaningful and scalable comparisons across different scenarios. The model employed a realistic saddle-shaped potential to mimic the confining electrostatics of a split-gate QPC, with tunable parameters such as ω_y/ω_x to control the strength of transverse and longitudinal confinement.

The initial results demonstrated the emergence of quantised conductance steps at integer multiples of $2e^2/h$, highlighting the role of mode formation and activation in defining the staircase profile. This basic quantisation was shown to depend heavily on the sharpness and separation of the transverse modes, which are in turn controlled by the confinement ratio. Simulations confirmed that increasing the ratio ω_y/ω_x produces more clearly defined steps and wider plateaus, improving both quantisation visibility and system stability. These findings align with experimental observations and reinforce the theoretical expectations that well-defined electrostatic confinement is critical for high-fidelity conductance quantisation.

A particularly valuable contribution of this project is the visualisation of how external fields modulate the energy landscape. In-plane magnetic fields were found to lift spin degeneracy via the Zeeman effect, resulting in the characteristic splitting of conductance steps into half-integer plateaus of e^2/h . This was supported by differential conductance maps, which captured these transitions with high precision and allowed for visual indexing of spin-resolved subbands. Similarly, perpendicular magnetic fields induced cyclotron motion and Landau level formation, effectively sharpening the energy spacing between conducting modes as well as enforcing system stability. This behaviour reflects a transition from electrostatic to magnetically governed confinement and provides a deeper understanding of how quantum transport evolves under different field configurations.

The material-dependence study extended the model to incorporate realistic values of effective mass and Landé g -factor for various semiconductors, showing how intrinsic material properties influence mode spacing and spin splitting. Lighter effective masses yielded sharper subband transitions due to enhanced confinement, while larger g values amplified the Zeeman splitting. These simulations offered strong theoretical insight into why materials such as InSb exhibit pronounced spin-resolved conductance features, and why others like Si or GaAs display more subtle effects. This analysis demonstrates the importance of material selection in device design, especially for spintronic or quantum applications.

where control over spin channels is crucial.

Temperature-dependent behaviour was also explored in depth. The study illustrated how increasing temperature gradually smooths out the quantised conductance steps due to thermal broadening of the Fermi-Dirac distribution. At low temperatures (e.g., 100 mK), conductance remains well-quantised, closely resembling the idealised $T = 0$ K case. However, at elevated temperatures, especially above 10 K and dramatically at 50 K, the steps become increasingly washed out. The simulation quantitatively captured this behaviour by tracking the full-width at half-maximum of the first conductance step, which increased with temperature, confirming the theoretical expectation that thermal excitation reduces quantisation clarity. This aligns with experimental findings and highlights the need for cryogenic conditions when attempting to observe or exploit quantised transport phenomena.

Importantly, the simulation framework developed in MATLAB proved to be flexible, modular, and well-suited to a wide range of parametric studies. However, as discussed in the future work section, this approach could be significantly enhanced by transitioning to more advanced quantum transport software such as *Kwant*. This would allow for the inclusion of arbitrary geometries, magnetic textures, disorder effects, and spin-orbit coupling, enabling the exploration of even more complex and experimentally relevant systems. Given the rising popularity of *Kwant* in mesoscopic physics and nanotechnology research, integrating it with the existing methodology offers a promising path forward.

Overall, this project has fulfilled its primary objective of visualising and analysing quantised conductance in low-dimensional semiconductor systems. It has provided detailed insight into the interplay between confinement, magnetic field effects, material parameters, and thermal fluctuations. The results are consistent with both theoretical models and experimental observations, confirming the robustness and reliability of the simulation approach. Beyond technical achievements, the work also serves as a valuable teaching tool for understanding mesoscopic transport and lays a strong foundation for future research into quantum coherent devices.

In the context of emerging quantum technologies, where precise control over electron flow, spin states, and energy modes is paramount, the knowledge gained from this study holds significant value. As device dimensions continue to shrink and quantum effects become dominant, the ability to simulate and predict conductance behaviour under realistic conditions will be instrumental in guiding design choices. Whether in quantum computing, spintronics, or nanoelectronic metrology, the ability to engineer and tune quantised conductance with high fidelity is set to play a central role—and this project provides a meaningful step toward that goal.

7 References

References

- [1] B. Roostaei, “Novel phenomena in confined electronic systems,” Ph.D. Thesis, Jan. 2007, accessed: 2 February 2025.
- [2] “Modulation doping - an overview,” <https://www.sciencedirect.com/topics/physics-and-astronomy/modulation-doping>, accessed: 2025-04-02.
- [3] Z. Zhang, J. Ran, F. Gao, and X. Guo, “Operation of single-spin qubits: Recent advances and prospects,” *Advanced Physics Research*, February 2025.
- [4] A. Gritsch, A. Ulanowski, J. Pforr, and A. Reiserer, “Optical single-shot readout of spin qubits in silicon,” *Nature Communications*, vol. 16, no. 1, p. 72, 2025.
- [5] “Quantum metrology - an overview,” <https://www.sciencedirect.com/topics/physics-and-astronomy/quantum-metrology>.
- [6] K. Delfanazari, J. Li, Y. Xiong, P. Ma, R. K. Puddy, T. Yi, I. Farrer, S. Komori, J. W. A. Robinson, L. Serra, D. A. Ritchie, M. J. Kelly, H. J. Joyce, and C. G. Smith, “Quantized conductance in hybrid split-gate arrays of superconducting quantum point contacts with semiconducting two-dimensional electron systems,” *Physical Review Applied*, vol. 21, no. 1, p. 014051, 2024. [Online]. Available: <https://journals.aps.org/prapplied/abstract/10.1103/PhysRevApplied.21.014051>
- [7] J. Feng, H. F. Legg, M. Bagchi, D. Loss, J. Klinovaja, and Y. Ando, “Long-range crossed andreev reflection in a topological insulator nanowire proximitized by a superconductor,” *Nature Physics*, March 2025. [Online]. Available: <https://www.nature.com/articles/s41567-025-02806-y>
- [8] P. Moles, F. Domínguez-Adame, and L. Chico, “Impact of vacancies on twisted bilayer graphene quantum point contacts,” *Physical Review B*, vol. 109, no. 4, p. 045415, 2024. [Online]. Available: <https://journals.aps.org/prb/abstract/10.1103/PhysRevB.109.045415>
- [9] M. Masseroni, M. Gull, A. Panigrahi, N. Jacobsen, F. Fischer, C. Tong, J. D. Gerber, M. Niese, T. Taniguchi, K. Watanabe, L. Levitov, T. Ihn, K. Ensslin, and H. Duprez, “Spin-orbit proximity in mos_2 /bilayer graphene heterostructures,” *Nature Communications*, vol. 15, p. 9251, 2024, published: 26 October 2024. [Online]. Available: <https://www.nature.com/articles/s41467-024-53324-z>
- [10] B. J. van Wees, H. van Houten, C. W. J. Beenakker, J. G. Williamson, L. P. Kouwenhoven, D. van der Marel, and C. T. Foxon, “Quantized conductance of point contacts in a two-dimensional electron gas,” *Physical Review Letters*, vol. 60, no. 9, pp. 848–850, 1988.
- [11] D. A. Wharam, T. J. Thornton, R. Newbury, M. Pepper, H. Ahmed, J. E. F. Frost, D. G. Hasko, D. C. Peacock, D. A. Ritchie, and G. A. C. Jones, “One-dimensional transport and the quantisation of the ballistic resistance,” *Journal of Physics C: Solid State Physics*, vol. 21, no. 8, pp. L209–L214, 1988.

- [12] M. Büttiker, “Quantized transmission of a saddle-point constriction,” *Physical Review B*, vol. 41, no. 11, April 1990.
- [13] C. Kastl, M. Stallhofer, D. Schuh, W. Wegscheider, and A. W. Holleitner, “Optoelectronic transport through quantum hall edge states,” *New Journal of Physics*, vol. 17, no. 2, p. 023007, February 2015.
- [14] S. Kumar and M. Pepper, “Interactions and non-magnetic fractional quantization in one-dimension,” *Applied Physics Letters*, vol. 119, no. 11, p. 110502, 2021.
- [15] S.-C. Ho, H.-J. Chang, C.-H. Chang, S.-T. Lo, G. Creeth, S. Kumar, I. Farrer, D. Ritchie, J. Griffiths, G. Jones, M. Pepper, and T.-M. Chen, “Imaging the zigzag wigner crystal in confinement-tunable quantum wires,” *Physical Review Letters*, vol. 121, no. 10, p. 106801, 2018. [Online]. Available: <https://journals.aps.org/prl/abstract/10.1103/PhysRevLett.121.106801>
- [16] H. Montagu, I. Farrer, D. Ritchie, and S. Kumar, “Spin polarised quantum conductance in 1d channels,” *Applied Physics Express*, vol. 18, no. 1, p. 015002, 2025, published online: 30 January 2025. [Online]. Available: <https://doi.org/10.35848/1882-0786/adac27>
- [17] H. van Houten and C. Beenakker, “Quantum point contacts,” *Physics Today*, vol. 49, no. 7, p. 22, 1996, originally published in abbreviated form in *Physics Today*, July 1996. Full version reprinted December 2005.
- [18] S. Kumar, K. J. Thomas, L. W. Smith, M. Pepper, G. L. Creeth, I. Farrer, D. Ritchie, G. Jones, and J. Griffiths, “Many-body effects in a quasi-one-dimensional electron gas,” *Physical Review B*, vol. 90, no. 20, p. 201304, 2014. [Online]. Available: <https://journals.aps.org/prb/abstract/10.1103/PhysRevB.90.201304>
- [19] A. G. Pogosov, A. A. Shevyrin, D. A. Pokhabov, E. Y. Zhdanov, and S. Kumar, “Suspended semiconductor nanostructures: physics and technology,” *Journal of Physics: Condensed Matter*, vol. 34, no. 26, p. 263001, 2022, published: 25 April 2022. [Online]. Available: <https://doi.org/10.1088/1361-648X/ac6308>
- [20] D. T. Park, S. Lee, U. Kim, H. Choi, and H. K. Choi, “Robust quantum point contact via trench gate modulation,” *Scientific Reports*, 2023. [Online]. Available: <https://www.nature.com/articles/s41598-023-43152-y>
- [21] S. Kumar, M. Pepper, H. Montagu, D. Ritchie, I. Farrer, J. Griffiths, and G. Jones, “Engineering electron wavefunctions in asymmetrically confined quasi one-dimensional structures,” *Applied Physics Letters*, vol. 118, no. 12, p. 124002, 2021, published online: 22 March 2021. [Online]. Available: <https://doi.org/10.1063/5.0045702>
- [22] S. Kumar, M. Pepper, S. N. Holmes, H. Montagu, Y. Gul, D. A. Ritchie, and I. Farrer, “Zero-magnetic field fractional quantum states,” *Physical Review Letters*, vol. 122, no. 8, p. 086803, 2019. [Online]. Available: <https://journals.aps.org/prl/abstract/10.1103/PhysRevLett.122.086803>

- [23] C. Yan, S. Kumar, K. Thomas, P. See, I. Farrer, D. Ritchie, J. Griffiths, G. Jones, and M. Pepper, "Engineering the spin polarization of one-dimensional electrons," *Journal of Physics: Condensed Matter*, vol. 30, no. 8, p. 08LT01, 2018, published: 30 January 2018. [Online]. Available: <https://doi.org/10.1088/1361-648X/aaa7ce>
- [24] N. Bhandari, P. P. Das, M. Cahay, R. S. Newrock, and S. T. Herbert, "Observation of a 0.5 conductance plateau in asymmetrically biased gaas quantum point contact," *Applied Physics Letters*, vol. 101, no. 10, p. 102401, 2012, published: 4 September 2012. [Online]. Available: <https://doi.org/10.1063/1.4749817>
- [25] University of Central Florida, "Motion of a charged particle in a magnetic field," 2016. [Online]. Available: <https://pressbooks.online.ucf.edu/osuniversityphysics2/chapter/motion-of-a-charged-particle-in-a-magnetic-field/>
- [26] S. Datta, *Electronic Transport in Mesoscopic Systems*. Cambridge University Press, 1995.
- [27] N. A. Bhandari, J. Charles, M. Dutta, and M. Cahay, "Steps toward an all-electric spin valve using side-gated quantum point contacts with lateral spin-orbit coupling," *Advances in Natural Sciences: Nanoscience and Nanotechnology*, vol. 4, no. 1, p. 013002, 2013, published: January 2013. [Online]. Available: <https://www.researchgate.net/publication/258311163>
- [28] J. H. Davies, I. A. Larkin, and E. V. Sukhorukov, "Modeling the patterned two-dimensional electron gas: Electrostatics," *Journal of Applied Physics*, vol. 77, no. 9, pp. 4504–4512, 1995. [Online]. Available: <https://doi.org/10.1063/1.359446>
- [29] O. Rossokhaty, "Non-equilibrium transport in electron solids," Ph.D. Thesis, The University of British Columbia, Vancouver, Canada, Dec. 2016, submitted to the Faculty of Graduate and Postdoctoral Studies (Physics).
- [30] V. Chabasseur-Molyneux, A. S. Dzurak, A. Kozorezov, J. K. Wigmore, D. A. Ritchie, A. C. Churchill, and M. Pepper, "Observation of the effect of electron-electron scattering on the impurity-limited resistivity of a two-dimensional electron gas," *Physical Review B*, vol. 51, no. 19, pp. 14 395–14 398, 1995, published: 15 May 1995. [Online]. Available: <https://doi.org/10.1103/PhysRevB.51.14395>
- [31] S. D. Sarma, S. Adam, E. H. Hwang, and E. Rossi, "Electronic transport in two-dimensional graphene," *Reviews of Modern Physics*, vol. 83, no. 2, pp. 407–470, April–June 2011. [Online]. Available: <https://doi.org/10.1103/RevModPhys.83.407>
- [32] M. Yama, M. Tatsuno, T. Kato, and M. Matsuo, "Spin pumping of two-dimensional electron gas with rashba and dresselhaus spin-orbit interactions," *Physical Review B*, vol. 104, no. 5, p. 054410, 2021, published: 6 August 2021. [Online]. Available: <https://doi.org/10.1103/PhysRevB.104.054410>

8 Appendices

8.1 Appendix A: MATLAB Code for Saddle-Point Potential (Figure 5)

```
V0 = 0;
m = 9.11e-31;
omega_x = 3e12;
omega_y = 8e12;

x = linspace(-3e-8, 3e-8, 200);
y = linspace(-1e-8, 1e-8, 200);
[X, Y] = meshgrid(x, y);

V = V0 - 0.5 * m * omega_x^2 .* X.^2 + 0.5 * m * omega_y^2 .* Y
    .^2;

figure;
surf(X, Y, V, 'EdgeColor', 'k');
xlabel('$x$-(m)', 'Interpreter', 'latex');
ylabel('$y$-(m)', 'Interpreter', 'latex');
zlabel('$V(x,y)$-(J)', 'Interpreter', 'latex');
colorbar;
view([-30, 50]);
zlim([-2e-20, 2e-20]);
axis tight;
shading interp;
title('Saddle-Potential');
```

8.2 Appendix B: MATLAB Code for Split-Gate Potential Profile (Figure 6)

```
x = linspace(0, 1200, 300);
y = linspace(0, 500, 300);
[X, Y] = meshgrid(x, y);

energy = (0.04 * exp(-(X-600).^2 + (Y-0).^2)/(2*100^2)) + ...
         0.04 * exp(-(X-600).^2 + (Y-500).^2)/(2*100^2)) .*
         ...
         (X > 0) .* (Y > 0) .* (X < 1200) .* (Y < 500);

figure;
contourf(X, Y, energy, 100, 'LineStyle', 'none');
colormap('parula');
c = colorbar;
ylabel(c, 'eV', 'Interpreter', 'latex');
caxis([0 0.03]);

xlabel('X-Position (nm)', 'Interpreter', 'latex');
ylabel('Y-Position (nm)', 'Interpreter', 'latex');
hold on;
plot([400, 800], [250, 250], 'w—', 'LineWidth', 2);
pbaspect([1200 500 1]);
xlim([0 1200]);
ylim([0 500]);
title('Split-Gate-Potential-Profile');
hold off;
```

8.3 Appendix C: MATLAB Code for Fermi Energy and Thresholds (Figure 7)

```
V0 = 1e-20;
hbar = 1.0545718e-34;
omega_y = 1e13;
EF = 1.5e-20;

n_max = 10;
n = 0:n_max;

E_n = V0 + hbar * omega_y * (n + 0.5);

open_channels = E_n <= EF;
closed_channels = E_n > EF;

figure;
hold on;
stem(n(open_channels), E_n(open_channels), 'g', 'LineWidth', 2,
     'DisplayName', 'Open-Channels');
stem(n(closed_channels), E_n(closed_channels), 'r', 'LineWidth',
     2, 'DisplayName', 'Closed-Channels');
xlabel('Mode-Index-(n)', 'Interpreter', 'latex');
ylabel('Energy-$E_n$-(J)', 'Interpreter', 'latex');
yline(EF, 'b—', 'Fermi-Energy-$E_F$', 'Interpreter', 'latex', '
     LineWidth', 1.5, 'HandleVisibility', 'off');
legend('Location', 'best');
title('Fermi-Energy-Channel-Transmission');
grid on;
hold off;
```

8.4 Appendix D: MATLAB Code for Transmission Probabilities and Total Conductance (Figure 8)

```

set(groot, 'DefaultAxesTickLabelInterpreter', 'latex');
set(groot, 'DefaultLegendInterpreter', 'latex');
set(groot, 'DefaultTextInterpreter', 'latex');
V0 = 1e-20;
hbar = 1.0545718e-34;
e = 1.60217662e-19;
omega_x = 1e13;
omega_y = 3e13;
E_scaled = linspace(0, 12, 500);
n_max = 3;
n = 0:n_max;
T = zeros(length(n), length(E_scaled));
G = zeros(1, length(E_scaled));

for i = 1:length(E_scaled)
    E = E_scaled(i) * hbar * omega_x + V0;
    for j = 1:length(n)
        epsilon_n = 2 * (E - hbar * omega_y * (n(j) + 0.5) - V0)
            / (hbar * omega_x);
        T(j, i) = 1 / (1 + exp(-pi * epsilon_n));
    end
    G(i) = sum(T(:, i)) * (2*e^2 / hbar);
end

figure;
hold on;

for j = 1:length(n)
    plot(E_scaled, T(j, :), 'LineWidth', 1.2, ...
        'DisplayName', sprintf('$T_{%d%d}$', n(j), n(j)));
end

plot(E_scaled, G / (2*e^2 / hbar), 'k', 'LineWidth', 1.5, ...
    'DisplayName', '$G$');

xlabel('$ (E - V_0) / \hbar \omega_x $', 'Interpreter', 'latex', 'FontSize', 16);
ylabel('$ G \cdot (e^2 / h) $', 'Interpreter', 'latex', 'FontSize', 16);
legend('Location', 'best', 'FontSize', 14);
grid on;
hold off;
title('Quantised Conductance & Sum of Modes', 'Interpreter', 'latex', 'FontSize', 16);

```

8.5 Appendix E: MATLAB Code for Varying ω_y/ω_x (Figure 10)

```
V0 = 1e-20;
hbar = 1.0545718e-34;
e = 1.60217662e-19;
omega_x = 1e13;

E_scaled = linspace(-2, 8, 500);

n_max = 10;
n = 0:n_max;

omega_y_ratios = [1, 2, 3, 4];

figure;

for k = 1:length(omega_y_ratios)
    omega_y_ratio = omega_y_ratios(k);
    omega_y = omega_y_ratio * omega_x;
    G = zeros(1, length(E_scaled));

    for i = 1:length(E_scaled)
        E = E_scaled(i) * hbar * omega_x + V0;
        for j = 1:length(n)
            epsilon_n = 2 * (E - hbar * omega_y * (n(j) + 0.5) -
                V0) / (hbar * omega_x);
            T_n = 1 / (1 + exp(-pi * epsilon_n));
            G(i) = G(i) + T_n * (e^2 / hbar);
        end
    end

    subplot(2, 2, k);
    plot(E_scaled, G / (e^2 / hbar), 'b', 'LineWidth', 1.5);
    xlabel('$$(E-V_0)/\hbar\omega_x$', 'Interpreter', 'latex', 'FontSize', 10);
    ylabel('$G/(e^2/h)$', 'Interpreter', 'latex', 'FontSize', 10);
    title(sprintf('$\\omega_y/-\\omega_x=\\%d$', omega_y_ratio),
        'Interpreter', 'latex', 'FontSize', 12);
    xlim([-2, 8]);
    ylim([0, 4]);
    grid on;
end

sgtitle('Quantised Conductance Varying $\\omega_y$ with Constant $\\omega_x$',
    'Interpreter', 'latex', 'FontSize', 16);
```


8.6 Appendix F: MATLAB Code for Varying ω_x/ω_y (Figure 11)

```
V0 = 1e-20;
hbar = 1.0545718e-34;
e = 1.60217662e-19;
omega_y = 3e13;

E_scaled = linspace(-2, 8, 500);

n_max = 10;
n = 0:n_max;

omega_x_ratios = [1, 2, 3, 4];

figure;

for k = 1:length(omega_x_ratios)
    omega_x_ratio = omega_x_ratios(k);
    omega_x = omega_x_ratio * omega_y;
    G = zeros(1, length(E_scaled));

    for i = 1:length(E_scaled)
        E = E_scaled(i) * hbar * omega_y + V0;
        for j = 1:length(n)
            epsilon_n = 2 * (E - hbar * omega_y * (n(j) + 0.5) -
                V0) / (hbar * omega_x);
            T_n = 1 / (1 + exp(-pi * epsilon_n));
            G(i) = G(i) + T_n * (e^2 / hbar);
        end
    end

    subplot(2, 2, k);
    plot(E_scaled, G / (e^2 / hbar), 'b', 'LineWidth', 1.5);
    xlabel('$ (E - V_0) / \hbar \omega_y $', 'Interpreter', 'latex', 'FontSize', 10);
    ylabel('$ G / (e^2 / h) $', 'Interpreter', 'latex', 'FontSize', 10);
    title(sprintf('$ \omega_x / \omega_y = %d $', omega_x_ratio), 'Interpreter', 'latex', 'FontSize', 12);
    xlim([-2, 8]);
    ylim([0, 4]);
    grid on;
end

sgtitle('Quantised Conductance Varying $ \omega_x $ with Constant $ \omega_y $', 'Interpreter', 'latex', 'FontSize', 16);
```

8.7 Appendix G: MATLAB Code for Quantised Conductance vs ω_y/ω_x (Figure 12)

```
V0 = 1e-20;
hbar = 1.0545718e-34;
e = 1.60217662e-19;
omega_x = 1e13;

E_scaled = linspace(-2, 8, 500);
n_max = 10;
n = 0:n_max;
omega_y_ratios = linspace(0.5, 5, 10);

colors = jet(length(omega_y_ratios));
figure;
hold on;
legend_entries = cell(length(omega_y_ratios), 1);

for k = 1:length(omega_y_ratios)
    omega_y = omega_y_ratios(k) * omega_x;
    G = zeros(1, length(E_scaled));

    for i = 1:length(E_scaled)
        E = E_scaled(i) * hbar * omega_x + V0;
        for j = 1:length(n)
            epsilon_n = 2 * (E - hbar * omega_y * (n(j) + 0.5) -
                V0) / (hbar * omega_x);
            T_n = 1 / (1 + exp(-pi * epsilon_n));
            G(i) = G(i) + T_n * (e^2 / hbar);
        end
    end

    plot(E_scaled, G / (e^2 / hbar), 'Color', colors(k, :), '
        LineWidth', 1.2);
    legend_entries{k} = sprintf('$\\omega_y/-\\omega_x=\\%.1f$',
        omega_y_ratios(k));
end

xlabel('$ (E-V_0) / -\\hbar\\omega_x$', 'Interpreter', 'latex', '
    FontSize', 14);
ylabel('$G / -(e^2 / -h)$', 'Interpreter', 'latex', 'FontSize',
    14);
xlim([-2, 8]);
ylim([0, 4]);
grid on;
legend(legend_entries, 'Location', 'best', 'Interpreter', 'latex
    ');
hold off;
```

8.8 Appendix H: MATLAB Code for Transmission Probabilities (Figure 13)

```
V0 = 1e-20;
hbar = 1.0545718e-34;
e = 1.60217662e-19;
omega_x = 1e13;
omega_y = 3e13;

E_scaled = linspace(0, 12, 500);

n_max = 3;
n = 0:n_max;

G_full = zeros(1, length(E_scaled));
G_80 = zeros(1, length(E_scaled));
G_60 = zeros(1, length(E_scaled));
G_40 = zeros(1, length(E_scaled));

for i = 1:length(E_scaled)
    E = E_scaled(i) * hbar * omega_x + V0;
    G_i_full = 0;
    G_i_80 = 0;
    G_i_60 = 0;
    G_i_40 = 0;
    for j = 1:length(n)
        epsilon_n = 2 * (E - hbar * omega_y * (n(j) + 0.5) - V0)
            / (hbar * omega_x);
        T_base = 1 / (1 + exp(-pi * epsilon_n));
        T_full = T_base * 1.0;
        T_80 = T_base * 0.8;
        T_60 = T_base * 0.6;
        T_40 = T_base * 0.4;
        G_i_full = G_i_full + T_full * (e^2 / hbar);
        G_i_80 = G_i_80 + T_80 * (e^2 / hbar);
        G_i_60 = G_i_60 + T_60 * (e^2 / hbar);
        G_i_40 = G_i_40 + T_40 * (e^2 / hbar);
    end
    G_full(i) = G_i_full;
    G_80(i) = G_i_80;
    G_60(i) = G_i_60;
    G_40(i) = G_i_40;
end

figure;
hold on;
plot(E_scaled, G_full / (e^2 / hbar), 'Color', [0 0.4470
    0.7410], 'LineWidth', 1.5, 'DisplayName', '$T=100\%$');
```

```

plot(E_scaled, G_80 / (e^2 / hbar), 'Color', [0.8500 0.3250
    0.0980], 'LineStyle', '—', 'LineWidth', 1.5, 'DisplayName', '
    $T=80\%$');
plot(E_scaled, G_60 / (e^2 / hbar), 'Color', [0.9290 0.6940
    0.1250], 'LineStyle', ':', 'LineWidth', 1.5, 'DisplayName', '
    $T=60\%$');
plot(E_scaled, G_40 / (e^2 / hbar), 'Color', [0.4940 0.1840
    0.5560], 'LineStyle', '—.', 'LineWidth', 1.5, 'DisplayName', '
    $T=40\%$');
xlabel('$(E-V_0)/\hbar\omega_x$', 'Interpreter', 'latex', '
    FontSize', 16);
ylabel('$G/(e^2/h)$', 'Interpreter', 'latex', 'FontSize',
    16);
legend('Interpreter', 'latex', 'FontSize', 14, 'Location', 'best
    ');
title('Practical-Transmission-Probabilities');
grid on;
hold off;

```

8.9 Appendix I: MATLAB Code for In-Plane Magnetic Field Conductance (Figure 14)

```
V0 = 1e-20;
hbar = 1.0545718e-34;
e = 1.60217662e-19;
m = 0.067 * 9.10938356e-31;
omega_x = 1e13;
omega_y = 4 * omega_x;

E_scaled = linspace(-4, 20, 500);

n_max = 10;
n = 0:n_max;

g = 2;
mu_B = e * hbar / (2 * m);

B_values = [0, 5, 10, 15];

figure;
hold on;

for B_index = 1:length(B_values)
    B = B_values(B_index);
    G = zeros(1, length(E_scaled));

    for i = 1:length(E_scaled)
        E = E_scaled(i) * hbar * omega_x + V0;
        G_spin_up = 0;
        G_spin_down = 0;

        for s = [-1, 1]
            E_Zeeman = s * (g * mu_B * B) / 2;

            for j = 1:length(n)
                E_level = hbar * omega_y * (n(j) + 0.5) + V0 +
                    E_Zeeman;
                epsilon_n = (E - E_level) / (hbar * omega_x);
                T_n = 1 / (1 + exp(-pi * epsilon_n));

                if s == 1
                    G_spin_up = G_spin_up + T_n * (e^2 / hbar);
                else
                    G_spin_down = G_spin_down + T_n * (e^2 /
                        hbar);
                end
            end
        end
    end
end
```

```

        end
    end

    G(i) = G_spin_up + G_spin_down;
end

plot(E_scaled, G / (2 * e^2 / hbar), 'LineWidth', 1.5, ...
      'DisplayName', sprintf('$B_{\parallel} = %.1f$ T', B))
;
end

xlabel('(E - V_0) / \hbar \omega_x$', 'Interpreter', 'latex', 'FontSize', 14);
ylabel('$G / (2e^2 / h)$', 'Interpreter', 'latex', 'FontSize', 14);
xlim([-2, 20]);
ylim([0, 5]);
grid on;
legend('show', 'Location', 'best', 'Interpreter', 'latex', 'FontSize', 12);
hold off;

```

8.10 Appendix J: MATLAB Code for Perpendicular Magnetic Field Conductance (Figure 16)

```
V0 = 1e-20;
hbar = 1.0545718e-34;
e = 1.60217662e-19;
m = 9.10938356e-31;
omega_x = 1e13;
omega_y = 1.0 * omega_x;

E_scaled = linspace(-4, 10, 500);

n_max = 10;
n = 0:n_max;

omega_c_ratios = linspace(0, 5, 21);

colors = jet(length(omega_c_ratios));

B_base = 1;
l_B = sqrt(hbar / (e * B_base));

figure;
hold on;

for k = 1:length(omega_c_ratios)
    omega_c = abs(omega_c_ratios(k) * omega_x);
    G = zeros(1, length(E_scaled));

    for i = 1:length(E_scaled)
        E = E_scaled(i) * hbar * omega_x + V0;

        for j = 1:length(n)
            if omega_c > 0
                E1 = (hbar * omega_x * omega_y) / (2 * omega_c);
                E2 = hbar * omega_c;
            else
                E1 = 0;
                E2 = 0;
            end

            if E1 > 0 && E2 > 0
                epsilon_n = (E - E2 * (n(j) + 0.5) - V0) / E1;
                T_n = 1 / (1 + exp(-pi * epsilon_n));
                G(i) = G(i) + T_n * (e^2 / hbar);
            end
        end
    end
end
```

```

    end

    plot(E_scaled, G / (e^2 / hbar), 'Color', colors(k, :), '
        LineWidth', 1);
end

colormap(colors);
cbar = colorbar;
cbar.Ticks = linspace(0, 1, length(omega_c_ratios));
cbar.TickLabels = arrayfun(@(x) sprintf('%.2f', x),
    omega_c_ratios, 'UniformOutput', false);
cbar.Label.String = '\omega_c / \omega_x';
cbar.Label.Interpreter = 'tex';
cbar.Label.FontSize = 12;

xlabel('$ (E - V_0) / \hbar \omega_x $', 'Interpreter', 'latex', '
    FontSize', 14);
ylabel('$ G / (2e^2 / h) $', 'Interpreter', 'latex', 'FontSize',
    14);
xlim([-2, 10]);
ylim([0.01, 6]);
hold off;
grid on;
title('Quantised Conductance in Magnetic Field');

```


8.11 Appendix K: MATLAB Code for Effective Mass Dependence(Figure 17)

```
V0 = 1e-20;
hbar = 1.0545718e-34;
e = 1.60217662e-19;
omega_x = 1e13;
omega_y = 4 * omega_x;

E_scaled = linspace(-4, 20, 500);

n_max = 10;
n = 0:n_max;

B = 10;

effective_masses = [0.19, 0.0135, 0.041, 0.067, 0.5] *
    9.10938356e-31;
materials = {'Si--electrons', 'InSb--electrons', 'InGaAs--
    electrons', ...
    'GaAs--electrons', 'GaAs--holes'};

figure;
hold on;

for m_index = 1:length(effective_masses)
    m = effective_masses(m_index);
    mu_B = e * hbar / (2 * m);

    G = zeros(1, length(E_scaled));

    for i = 1:length(E_scaled)
        E = E_scaled(i) * hbar * omega_x + V0;

        G_spin_up = 0;
        G_spin_down = 0;

        for s = [-1, 1]
            E_Zeeman = s * (2 * mu_B * B) / 2;

            for j = 1:length(n)
                E_level = hbar * omega_y * (n(j) + 0.5) + V0 +
                    E_Zeeman;
                epsilon_n = (E - E_level) / (hbar * omega_x);
                T_n = 1 / (1 + exp(-pi * epsilon_n));

                if s == 1
                    G_spin_up = G_spin_up + T_n * (e^2 / hbar);
```

```

        else
            G_spin_down = G_spin_down + T_n * (e^2 /
                hbar);
        end
    end
end

G(i) = G_spin_up + G_spin_down;
end

plot(E_scaled, G / (2 * e^2 / hbar), 'LineWidth', 1.5, ...
    'DisplayName', sprintf('$m^* = %.3f \cdot m_e$-(%s)', m /
        9.10938356e-31, materials{m_index}));
end

xlabel('$ (E - V_0) / \hbar \omega_x$', 'Interpreter', 'latex', '
    FontSize', 14);
ylabel('$ G / (2e^2 / h) $', 'Interpreter', 'latex', 'FontSize',
    14);
xlim([-2, 20]);
ylim([0, 5]);
grid on;

legend('show', 'Location', 'best', 'Interpreter', 'latex', '
    FontSize', 12);

title('Quantised Conductance for Different Effective Masses ($B =
    10 \, \mathrm{T}, \omega_y / \omega_x = 4$)', ...
    'Interpreter', 'latex', 'FontSize', 14);
hold off;

```

8.12 Appendix L: MATLAB Code for Material-Dependent g -Factor (Figure 18)

```
V0 = 1e-20;
hbar = 1.0545718e-34;
e = 1.60217662e-19;
m = 0.067 * 9.10938356e-31;
omega_x = 1e13;
omega_y = 4 * omega_x;

E_scaled = linspace(-4, 20, 500);

n_max = 10;
n = 0:n_max;

B = 10;

g_values = [2.0, 1.6, -0.44, -14, -4.5, -51];
materials = {'Silicon-(Si)', 'Germanium-(Ge)', 'Gallium-Arsenide-
    -(GaAs)', ...
    'Indium-Arsenide-(InAs)', 'Indium-Gallium-Arsenide-
    (InGaAs)', ...
    'Indium-Antimonide-(InSb)'};

figure;
hold on;

for g_index = 1:length(g_values)
    g = g_values(g_index);
    mu_B = e * hbar / (2 * m);

    G = zeros(1, length(E_scaled));

    for i = 1:length(E_scaled)
        E = E_scaled(i) * hbar * omega_x + V0;

        G_spin_up = 0;
        G_spin_down = 0;

        for s = [-1, 1]
            E_Zeeman = s * (g * mu_B * B) / 2;

            for j = 1:length(n)
                E_level = hbar * omega_y * (n(j) + 0.5) + V0 +
                    E_Zeeman;
                epsilon_n = (E - E_level) / (hbar * omega_x);
                T_n = 1 / (1 + exp(-pi * epsilon_n));
```

```

        if s == 1
            G_spin_up = G_spin_up + T_n * (e^2 / hbar);
        else
            G_spin_down = G_spin_down + T_n * (e^2 /
                hbar);
        end
    end
end

G(i) = G_spin_up + G_spin_down;
end

plot(E_scaled, G / (2 * e^2 / hbar), 'LineWidth', 1.5, ...
    'DisplayName', sprintf('%s-(g=%0.1f)', materials{
        g_index}, g));
end

xlabel('$ (E - V_0) / \hbar \omega_x $', 'Interpreter', 'latex', '
    FontSize', 14);
ylabel('$ G / (2e^2 / h) $', 'Interpreter', 'latex', 'FontSize',
    14);
xlim([-2, 20]);
ylim([0, 5]);
grid on;

legend('show', 'Location', 'best', 'Interpreter', 'latex', '
    FontSize', 12);

title('Quantised Conductance for Bulk Semiconductors ($B = 10 \backslash \backslash
    \mathrm{T}, \omega_y / \omega_x = 4$)', ...
    'Interpreter', 'latex', 'FontSize', 14);
hold off;

```

8.13 Appendix M: MATLAB Code for GaAs Electron and Hole Configurations (Figure 19)

```
V0 = 1e-20;
hbar = 1.0545718e-34;
e = 1.60217662e-19;
m = 0.067 * 9.10938356e-31;
omega_x = 1e13;
omega_y = 4 * omega_x;

E_scaled = linspace(-4, 20, 500);

n_max = 10;
n = 0:n_max;

B = 10;

g_values = [-0.44, 3.6];
configurations = { 'GaAs-Electrons', 'GaAs-Holes' };

figure;
hold on;

for config_index = 1:length(g_values)
    g = g_values(config_index);
    mu_B = e * hbar / (2 * m);

    G = zeros(1, length(E_scaled));

    for i = 1:length(E_scaled)
        E = E_scaled(i) * hbar * omega_x + V0;

        G_spin_up = 0;
        G_spin_down = 0;

        for s = [-1, 1]
            E_Zeeman = s * (g * mu_B * B) / 2;

            for j = 1:length(n)
                E_level = hbar * omega_y * (n(j) + 0.5) + V0 +
                    E_Zeeman;
                epsilon_n = (E - E_level) / (hbar * omega_x);
                T_n = 1 / (1 + exp(-pi * epsilon_n));

                if s == 1
                    G_spin_up = G_spin_up + T_n * (e^2 / hbar);
                else

```

```

        G_spin_down = G_spin_down + T_n * (e^2 /
            hbar);
    end
end
end

G(i) = G_spin_up + G_spin_down;
end

plot(E_scaled, G / (2 * e^2 / hbar), 'LineWidth', 1.5, ...
    'DisplayName', sprintf('%s-(g=%0.1f)', configurations{
        config_index}, g));
end

xlabel('$ (E - V_0) / \hbar \omega_x $', 'Interpreter', 'latex', '
    FontSize', 14);
ylabel('$ G / (2e^2 / h) $', 'Interpreter', 'latex', 'FontSize',
    14);
xlim([-2, 20]);
ylim([0, 5]);
grid on;

legend('show', 'Location', 'best', 'Interpreter', 'latex', '
    FontSize', 12);

title('Quantised Conductance for GaAs Configurations ($B = 10 \backslash \backslash
    \mathrm{T} \backslash \backslash \omega_y / \backslash \omega_x = 4$)', ...
    'Interpreter', 'latex', 'FontSize', 14);
hold off;

```

8.14 Appendix N: MATLAB Code for Temperature Dependence (Figures 22, 28, 29)

```
V0 = 1e-20;
hbar = 1.0545718e-34;
e = 1.60217662e-19;
m = 0.067 * 9.10938356e-31;
omega_x = 1e13;
omega_y = 2 * omega_x;
k_B = 1.380649e-23;

E_scaled = linspace(-4, 20, 2000);
E_actual = E_scaled * hbar * omega_x + V0;

n_max = 10;
n = 0:n_max;

temperature_values = [0, 0.1, 0.5, 1, 2, 5, 10, 12, 15, 18, 20,
    50];
num_T = length(temperature_values);
offset_step = 2;
colors = parula(num_T);

G_all = zeros(num_T, length(E_scaled));
fwhm_values = zeros(1, num_T);

figure;
hold on;

for t_index = 1:num_T
    T = temperature_values(t_index);
    G = zeros(1, length(E_scaled));

    for i = 1:length(E_actual)
        E = E_actual(i);
        G_total = 0;

        for j = n
            E_n = hbar * omega_y * (j + 0.5) + V0;
            epsilon_n = (E - E_n) / (hbar * omega_x);
            T_n = 1 / (1 + exp(-pi * epsilon_n));

            if T > 0
                arg = (E_n - E) / (k_B * T);
                arg = max(min(arg, 700), -700);
                fermi = 1 / (1 + exp(arg));
            else
                fermi = double(E > E_n);
            end
        end
    end
end
```

```

        end

        G_total = G_total + fermi * T_n * (e^2 / hbar);
    end

    G(i) = G_total / (2 * e^2 / hbar);
end

if T > 0
    G = smoothdata(G, 'movmean', 3);
end

G_all(t_index, :) = G;

offset = (t_index - 1) * offset_step;
plot(E_scaled + offset, G, ...
     'Color', colors(t_index, :), 'LineWidth', 1.5, ...
     'DisplayName', sprintf('$T = %.1f$ K', T));

idx_half = find(G > 0.5, 1, 'first'):find(G > 0.5, 1, 'last'
);
if ~isempty(idx_half)
    fwhm_values(t_index) = E_scaled(idx_half(end)) -
        E_scaled(idx_half(1));
else
    fwhm_values(t_index) = NaN;
end
end

xlabel('$ (E - V_0) / \hbar \omega_x$', 'Interpreter', 'latex', '
    FontSize', 14);
ylabel('$ G / (2e^2/h) $', 'Interpreter', 'latex', 'FontSize', 14)
;
xlim([-2, 20 + (num_T - 1) * offset_step]);
ylim([0, 5]);
legend('show', 'Interpreter', 'latex', 'FontSize', 10, 'Location
    ', 'best');
grid on;
hold off;

exclude_index = find(temperature_values == 50);
fwhm_T = temperature_values;
fwhm_T(exclude_index) = [];
fwhm_plot = fwhm_values;
fwhm_plot(exclude_index) = [];

```



```

figure;
plot(fwhm_T, fwhm_plot, '-o', 'MarkerFaceColor', 'b', 'LineWidth',
    1.5);
xlabel('Temperature (K)', 'Interpreter', 'latex', 'FontSize',
    14);
ylabel('FWHM of First Conductance Step', 'Interpreter', 'latex',
    'FontSize', 14);
xlim([0, 20]);
grid on;
hold off;

figure;
hold on;
E_mid = (E_scaled(1:end-1) + E_scaled(2:end)) / 2;
dG_dE = diff(G_all, 1, 2) ./ diff(E_scaled);

for t_index = 1:num_T
    if temperature_values(t_index) == 50
        continue;
    end
    offset = (t_index - 1) * offset_step;
    plot(E_mid + offset, dG_dE(t_index, :), ...
        'Color', colors(t_index, :), 'LineWidth', 1.5, ...
        'DisplayName', sprintf('$T = %.1f$ K',
            temperature_values(t_index)));
end

xlabel('$ (E - V_0) / \hbar \omega_x $', 'Interpreter', 'latex', '
    FontSize', 14);
ylabel('$dG/dE$', 'Interpreter', 'latex', 'FontSize', 14);
xlim([-2, 20 + (num_T - 1) * offset_step]);
legend('show', 'Interpreter', 'latex', 'FontSize', 12, 'Location',
    'best');
grid on;
hold off;

```

8.15 Appendix O: MATLAB Code for Transmission Derivative (Figure 23)

```
set(groot, 'DefaultAxesTickLabelInterpreter', 'latex');
set(groot, 'DefaultLegendInterpreter', 'latex');
set(groot, 'DefaultTextInterpreter', 'latex');

V0 = 1e-20;
hbar = 1.0545718e-34;
e = 1.60217662e-19;
omega_x = 1e13;
omega_y = 3e13;

E_scaled = linspace(0, 12, 500);
n_max = 3;
n = 0:n_max;

T = zeros(length(n), length(E_scaled));
G = zeros(1, length(E_scaled));

for i = 1:length(E_scaled)
    E = E_scaled(i) * hbar * omega_x + V0;
    for j = 1:length(n)
        epsilon_n = 2 * (E - hbar * omega_y * (n(j) + 0.5) - V0)
            / (hbar * omega_x);
        T(j, i) = 1 / (1 + exp(-pi * epsilon_n));
    end
    G(i) = sum(T(:, i)) * (2 * e^2 / hbar);
end

dT_dE = zeros(size(T));
for j = 1:size(T, 1)
    dT_dE(j, :) = gradient(T(j, :), E_scaled);
end

figure;
hold on;

for j = 1:length(n)
    plot(E_scaled, T(j, :), 'LineWidth', 1.2, 'HandleVisibility',
        'off');
end

plot(E_scaled, G / (e^2 / hbar), 'k', 'LineWidth', 1.5, '
    HandleVisibility', 'off');

yyaxis right
for j = 1:length(n)
```

```

    plot(E_scaled, dT_dE(j, :), '—', ...
        'DisplayName', sprintf('$\frac{dT_{%d}}{dE}$', n(j),
            n(j)), 'LineWidth', 1);
end

xlabel('$ (E - V_0) / \hbar \omega_x $', 'Interpreter', 'latex', 'FontSize', 16);
yyaxis left
ylabel('$ G \cdot (e^2 / h) $', 'Interpreter', 'latex', 'FontSize', 16);
yyaxis right
ylabel('$ \frac{dT}{dE} $', 'Interpreter', 'latex', 'FontSize', 16);
title('Transmission Derivative With Respect to Energy', 'Interpreter', 'latex', 'FontSize', 16);
grid on;
hold off;

```

8.16 Appendix P: MATLAB Code for Transmission Probability vs Mode Index (Figure 24)

```
V0 = 1e-20;
hbar = 1.0545718e-34;
omega_x = 1e13;
E = 2e-20;

n_max = 12;
n = 0:n_max;

omega_y_ratios = [1, 2, 3, 4];
colors = jet(length(omega_y_ratios));

figure;
hold on;

for idx = 1:length(omega_y_ratios)
    ratio = omega_y_ratios(idx);
    omega_y = ratio * omega_x;

    epsilon_n = 2 * (E - hbar * omega_y * (n + 0.5) - V0) / (
        hbar * omega_x);
    T_mn = 1 ./ (1 + exp(-pi * epsilon_n));

    plot(n, T_mn, 'o-', 'LineWidth', 1.5, ...
        'Color', colors(idx, :), ...
        'DisplayName', sprintf('$\\omega_y / \\omega_x = %.1f$',
            ratio));
end

xlabel('Mode-Index-(n)', 'Interpreter', 'latex');
ylabel('Transmission-Probability- $T_{mn}$ ', 'Interpreter', '
    latex');
legend('Location', 'best', 'Interpreter', 'latex');
grid on;
xlim([-1, n_max + 1]);
ylim([-0.1, 1.1]);

hold off;
```

8.17 Appendix Q: MATLAB Code for Transmission Derivative vs Confinement Ratio (Figure 25)

```
set(groot, 'DefaultAxesTickLabelInterpreter', 'latex');
set(groot, 'DefaultLegendInterpreter', 'latex');
set(groot, 'DefaultTextInterpreter', 'latex');
hbar = 1.0545718e-34;
omega_x = 1e13;
omega_y = 1e13;
omega_y_ratios = linspace(0.1, 5, 25);
dT_dE_y_over_x = zeros(size(omega_y_ratios));

for i = 1:length(omega_y_ratios)
    ratio = omega_y_ratios(i);
    dT_dE_y_over_x(i) = (4 * pi / (hbar * omega_x)) * exp(-2 *
        pi * ratio);
end

figure;
plot(omega_y_ratios, dT_dE_y_over_x, 'o-', 'LineWidth', 1.5);
xlabel('$\omega_y / \omega_x$', 'FontSize', 16);
ylabel('$\frac{dT}{dE}$', 'FontSize', 16);
title('Transmission Derivative vs $\omega_y / \omega_x$', '
    FontSize', 16);
xlim([0, max(omega_y_ratios) + 0.5]);
ylim([0, max(dT_dE_y_over_x) * 1.1]);
grid on;

omega_x_ratios = linspace(0.1, 5, 25);
dT_dE_x_over_y = zeros(size(omega_x_ratios));

for i = 1:length(omega_x_ratios)
    ratio = omega_x_ratios(i);
    omega_x_scaled = ratio * omega_y;
    dT_dE_x_over_y(i) = (4 * pi / (hbar * omega_x_scaled)) * exp
        (-2 * pi / ratio);
end

figure;
plot(omega_x_ratios, dT_dE_x_over_y, 'o-', 'LineWidth', 1.5);
xlabel('$\omega_x / \omega_y$', 'FontSize', 16);
ylabel('$\frac{dT}{dE}$', 'FontSize', 16);
title('Transmission Derivative vs $\omega_x / \omega_y$', '
    FontSize', 16);
xlim([min(omega_x_ratios), max(omega_x_ratios) + 0.5]);
ylim([0, max(dT_dE_x_over_y) * 1.1]);
grid on;
```

8.18 Appendix R: MATLAB Code for Indexed Differential Conductance vs In-Plane Magnetic Field (Figure 26)

```
V0 = 1e-20;
hbar = 1.0545718e-34;
e = 1.60217662e-19;
m = 0.067 * 9.10938356e-31;
omega_x = 1e13;
omega_y = 2 * omega_x;
g = 2;
mu_B = e * hbar / (2 * m);

E_scaled = linspace(-4, 20, 500);
E_actual = E_scaled * hbar * omega_x + V0;

n_max = 10;
n = 0:n_max;

B_values = 0:0.5:15;

G = zeros(length(B_values), length(E_scaled));

for b_index = 1:length(B_values)
    B = B_values(b_index);
    for i = 1:length(E_scaled)
        E = E_scaled(i);
        G_spin_up = 0;
        G_spin_down = 0;

        for s = [-1, 1]
            E_Zeeman = s * (g * mu_B * B) / 2;

            for j = n
                E_level = hbar * omega_y * (j + 0.5) + V0 +
                    E_Zeeman;
                epsilon_n = (E - E_level) / (hbar * omega_x);
                T_n = 1 / (1 + exp(-pi * epsilon_n));

                if s == 1
                    G_spin_up = G_spin_up + T_n * (e^2 / hbar);
                else
                    G_spin_down = G_spin_down + T_n * (e^2 /
                        hbar);
                end
            end
        end
    end
end
```

```

        G(b_index, i) = (G_spin_up + G_spin_down) / (2 * e^2 /
            hbar);
    end
end

[X, Y] = meshgrid(E_scaled, B_values);
differential_G = diff(G, 1, 2);
differential_G = [differential_G, differential_G(:, end)];

figure;
contourf(X, Y, differential_G, 50, 'LineStyle', 'none');
colormap('parula');
cbar = colorbar;
cbar.Label.String = 'Differential-Conductance-($dG/dE$)';
cbar.Label.Interpreter = 'latex';
cbar.Label.FontSize = 14;
caxis([0, max(differential_G(:))]);

xlabel('$ (E - V_0) / \hbar \omega_x $', 'Interpreter', 'latex', 'FontSize', 14);
ylabel('$ B_{\parallel} (T) $', 'Interpreter', 'latex', 'FontSize', 14);

```